Journal of Quantitative Spectroscopy & Radiative Transfer 111 (2010) 1426–1448

Contents lists available at ScienceDirect

Journal of Quantitative Spectroscopy & Radiative Transfer

journal homepage: www.elsevier.com/locate/jqsrt

A vector radiative transfer model of coupled ocean–atmosphere system using matrix-operator method for rough sea-surface

Xianqiang He *, Yan Bai, Qiankun Zhu, Fang Gong

State Key Laboratory of Satellite Ocean Environment Dynamics, Second Institute of Oceanography, State Oceanic Administration, Hangzhou, China

ARTICLE INFO

Article history:
Received 26 January 2010
Received in revised form
23 February 2010
Accepted 24 February 2010

Keywords:
Radiative transfer
Matrix-operator method
Coupled ocean–atmosphere system
Rough sea surface
Ocean optics
Ocean color remote sensing

ABSTRACT

A vector radiative transfer model termed PCOART has been developed for the coupled ocean–atmosphere system, using the matrix-operator (or adding-doubling) method, which considers the rough sea-surface. The theoretical formulations of the solution of the vector radiative transfer equation of the coupled ocean–atmosphere system, and the reflection–transmission matrices and internal radiation sources for rough sea surface are described. The model intercomparison is performed for several radiative transfer problems in the atmosphere and ocean, and the results show that PCOART can exactly predict the radiance fields for both flat and rough sea surface. Also, the polarizing remote sensing data from POLDER is used to test the capacity of PCOART to simulate the polarization radiance at the top-of-atmosphere, which shows that PCOART can perfectly reproduce the linear polarization reflectance measured by POLDER. PCOART can not only simulate the total radiance field in the coupled ocean–atmosphere system with wind-induced rough sea surface but also predict the polarization radiance field both in the atmosphere and in the ocean, which can serve as a good tool for the ocean optics and ocean color remote sensing communities.

1. Introduction

Radiative transfer plays a fundamental role in oceanic optics and ocean color remote sensing, and the radiative transfer model describes the radiance transferring through the atmospheric and oceanic medium, by which the sensor onboard space-platform can receive the radiance containing the desirable ocean color information. In the past decades, more than twenty satellite ocean color remote sensors had been launched (http://www.ioccg.org/), including the widely used sensors, such as Sea-viewing Wide Field-of-view Sensor (SeaWiFS), Moderate-resolution Imaging Spectroradiometer (MODIS) and Medium Resolution Imaging Spectrometer (MERIS). Also, about fifteen new satellite ocean color remote sensors are planned to be launched before 2015 (http://www.ioccg.org/), including the Visible Infrared Imager Radiometer Suite (VIIRS), Ocean & Land Color Instrument (OLCI), Geostationary Ocean Color Imager (GOCI), Second-generation Global Imager (S-GLI), etc. All of these sensors have enhanced spectral and radiometric resolution compared with their predecessor—Coastal Zone Color Scanner (CZCS). In order to fully retrieve the atmospheric and oceanic information from the satellite measured spectral signal, the radiative transfer in the atmosphere and ocean must be understood very well, e.g. the exact atmospheric correction of ocean color should be based on the vector radiative transfer in the atmosphere [1]. Meanwhile, the radiative transfer in the coupled ocean–atmosphere system is very important for the climate forecasting and for the marine biology [2]. However, the solution of the radiative transfer equation is complex, which should be based on the

* Corresponding author. Tel.: +86 571 81963117; fax: +86 571 81963112.
E-mail address: hexianqiang@sina.com (X. He).

0022-4073/$ - see front matter © 2010 Elsevier Ltd. All rights reserved.
doi:10.1016/j.jqsrt.2010.02.014

numerical method. To date, there are several different numerical methods for the solution of the radiative transfer equation. The most commonly used methods are the matrix-operator method (or adding-doubling method) [3], the discrete ordinates method [4], the spherical harmonic method [5], the Monte-Carlo solutions method [6], the invariant imbedding method [7], the method of *X* and *Y* functions [8], the successive orders of scattering method [9], the *FN* method [10], the finite elements method [11], etc.

Using these numerical methods, many codes have been developed for the application of atmospheric and oceanic radiative transfer problems. For example, DISORT for atmosphere [12] and Hydrolight for water [13] are one of the widely used codes to simulate the radiance fields in the atmosphere or ocean media. Simply, the code for solving the radiative transfer equation can be classified into the scalar and the vector one, the one solving the simple atmospheric (or simple ocean system) and the coupled ocean–atmosphere system, the one with flat sea surface and the one considering the rough sea surface, etc. All of these are related to the complexity of the numerical model. Theoretically, the closer the simulation to the real nature, the more complex the numerical model and code, but it is a challenge to solve the complicated radiative transfer equation and coding. In this paper, we would like to focus on the vector radiative transfer equation for the coupled ocean–atmospheric system with the consideration of the rough sea surface.

The solution for the vector radiative transfer equation in a coupled ocean–atmosphere system considering the rough sea surface is particularly of interest for the ocean optics and ocean color remote sensing. Polarization must be included in the accurate radiative transfer calculations at the surface of and within the ocean [14,15], and significant error can occur in radiance calculations when one neglects polarization effects [16–18]. Meanwhile, the polarization properties can be used to retrieve the ocean color information [19,20], and improve contrast in underwater viewing systems [21], and understand the effect of polarized light in the ocean on the behavior of marine organisms [22]. Also, the atmospheric correction of the ocean color remote sensing should consider the polarization; ignoring the polarization could induce $>10\%$ errors for the Rayleigh scattering calculation [23], so the polarization correction of the ocean color sensors should estimate the polarized radiance received by the sensor [24], such as the MODIS [25]. Usually the sea surface is ruffled by the wind. In order to obtain a realistic model of the atmosphere–ocean system, we need to solve the radiative transfer equation with the rough sea surface. However, there are few codes dealing with the vector radiative transfer of the coupled ocean–atmosphere system with the rough sea surface. Based on the matrix operator method, Nakajima and Tanaka [26] and Fischer and Grassl [27] solve the scalar radiative transfer equation in a coupled ocean–atmosphere system with wind-induced rough sea surface. Fell and Fischer have developed the scalar radiative transfer code named MOMO to deal with a coupled ocean–atmosphere system for the rough sea surface [28]. Jin and Stamnes have developed a website-based radiative transfer code named COART by solving the scalar radiative transfer equation in the coupled ocean–atmosphere system with a rough sea surface using the discrete ordinates method [29]. Bulgarelli et al. have developed the finite element method for solving the scalar radiative transfer equation in a coupled ocean–atmosphere system with a flat sea surface [30]. For the vector radiative transfer codes in the coupled ocean–atmosphere system, Chami et al. solved the vector radiative transfer equation using the successive orders of the scattering method, which assumes a flat ocean surface and ignores the circularly polarized component [31]. Recently, several vector radiative transfer models for coupled ocean–atmosphere system have been developed based on the successive order of the scattering method [32,33], the discrete ordinate method and the Monte-Carlo method [34–36]. To the best of the author's knowledge, the model by Chowdhary et al. is the only one that solves the vector radiative transfer equation in the coupled ocean–atmosphere system considering the rough sea surface based on the adding method [37].

We had developed a vector radiative transfer model of the coupled ocean–atmosphere system for flat sea surface using the matrix-operator method [38]. The code of the model for the vector radiative transfer in the atmosphere was based on the RT3 code developed by Evans and Stephens [39]. However, the flat surface assumption limits the applications of the model because the wind-blown ocean surface is hardly flat. Here, the aim of this paper is to develop a rather complete model trying to get close to the real nature, which is a vector radiative transfer model of the coupled ocean–atmosphere system for a rough sea surface. The model is termed as PCOART, which is based on our previous version for the flat sea surface [38]. In this paper, we describe the physics principle and detailed mathematical derivation of PCOART for rough sea-surface based on the previous version for the flat sea-surface. Firstly, we describe the vector radiative transfer equation, the detail mathematical derivation of matrix-operator method for simple atmosphere or ocean medium, and the coupling of the atmosphere and ocean radiative transfer. Then, we describe the detailed mathematical derivation of the reflection–transmission matrices, and the internal radiation sources for rough sea surface. Finally we provide the results of model validation and intercomparison. Section 4 presents the conclusions.

2. Theory

2.1. The vector radiative transfer equation

The radiation can be fully described by the Stokes vector $\mathbf{L}(=[I,Q,U,V]^T)$, where I, Q, U and V are the Stokes vector components, and the superscript T stands for the transpose of the vector. A formal definition of the Stokes vector components in a medium can be found in the literature [40]. The propagation and redistribution of the radiation in the

plane-parallel media such as atmosphere and ocean can be described by the vector radiative transfer equation as

$$\mu\frac{d\mathbf{L}(\tau;\mu,\phi)}{d\tau}=-\mathbf{L}(\tau;\mu,\phi)+\frac{\varpi(\tau)}{4\pi}\int_0^{2\pi}\int_{-1}^{1}\mathbf{Z}(\tau;\mu,\phi;\mu',\phi')\mathbf{L}(\tau;\mu',\phi')\,d\mu'\,d\phi'+\frac{\varpi(\tau)}{4\pi}\mathbf{Z}(\tau;\mu,\phi;\mu_0,\phi_0)\mathbf{F_0}\exp(-\tau/\mu_0) \tag{1}$$

where μ is the cosine of the zenith angle with the positive for downward and the minus for upward; ϕ is the azimuth angle; τ is the optical depth; ϖ is the single scattering albedo; $\mathbf{F}_0$ is the incident extraterrestrial solar flux vector, which should include the direct reflectance flux by the sea surface for the flat sea surface case; μ_0 and ϕ_0 are the cosine of solar zenith angle and azimuth angle, respectively. $\mathbf{Z}$ is the scattering phase matrix of the medium with 4×4 dimensions, which is defined as

$$\mathbf{Z}(\tau;\mu,\phi;\mu',\phi')=\mathbf{C}(\pi-i_2)\mathbf{P}(\tau;\mu,\phi;\mu',\phi')\mathbf{C}(-i_1) \tag{2}$$

where $\mathbf{C}$ is the rotation matrix that rotates the reference plane of the Stokes vector; i_1 and i_2 are the rotation angles [8]; and $\mathbf{P}$ is the scattering matrix for the turbid medium. Eq. (1) is valid for the macroscopically isotropic and mirror-symmetric scattering media at the visible and near-infrared wavelength where the thermal emission can be ignored [41].

2.2. The matrix-operator method for simple atmosphere or ocean medium

The matrix-operator (or adding-doubling) method is one of the most widely used methods to solve the radiative transfer equation in the plane-parallel medium such as atmosphere and ocean, and it is particularly suited for the development of remote sensing retrieval algorithms of cloud parameters and water constituents [41]. In the matrix-operator method, the azimuthally dependent Stokes vector and scattering phase matrix are expanded into the Fourier series as

$$\mathbf{L}(\tau;\mu,\phi)=\mathbf{L}^0(\tau;\mu)+\sum_{m=1}^{M}[\mathbf{L}^{cm}(\tau;\mu)\cos(m\phi)+\mathbf{L}^{sm}(\tau;\mu)\sin(m\phi)] \tag{3}$$

$$\mathbf{Z}(\tau;\mu,\phi;\mu',\phi')=\mathbf{Z}^0(\tau;\mu,\mu')+\sum_{m=1}^{M}\{\mathbf{Z}^{cm}(\tau;\mu,\mu')\cos[m(\phi-\phi')]+\mathbf{Z}^{sm}(\tau;\mu,\mu')\sin[m(\phi-\phi')]\} \tag{4}$$

Substituting Eqs. (3) and (4) into Eq. (1), and using the orthogonal properties of sine and cosine functions, we can obtain a series of $2M+1$ azimuthally independent equations as follows:

$$\mu\frac{d\mathbf{L}^0(\tau;\mu)}{d\tau}=-\mathbf{L}^0(\tau;\mu)+\frac{\varpi(\tau)}{2}\int_{-1}^{1}\mathbf{Z}^0(\tau;\mu,\mu')\mathbf{L}^0(\tau;\mu')\,d\mu'+\frac{\varpi(\tau)}{4\pi}\mathbf{Z}^0(\tau;\mu,\mu_0)\mathbf{F_0}\exp(-\tau/\mu_0) \tag{5}$$

$$\mu\frac{d\mathbf{L}^{cm}(\tau;\mu)}{d\tau}=-\mathbf{L}^{cm}(\tau;\mu)+\frac{\varpi(\tau)}{4}\int_{-1}^{1}[\mathbf{Z}^{cm}(\tau;\mu,\mu')\mathbf{L}^{cm}(\tau;\mu')-\mathbf{Z}^{sm}(\tau;\mu,\mu')\mathbf{L}^{sm}(\tau;\mu')]\,d\mu'+\frac{\varpi(\tau)}{4\pi}\mathbf{Z}^{cm}(\tau;\mu,\mu_0)\mathbf{F_0}\exp(-\tau/\mu_0) \tag{6}$$

$$\mu\frac{d\mathbf{L}^{sm}(\tau;\mu)}{d\tau}=-\mathbf{L}^{sm}(\tau;\mu)+\frac{\varpi(\tau)}{4}\int_{-1}^{1}[\mathbf{Z}^{sm}(\tau;\mu,\mu')\mathbf{L}^{cm}(\tau;\mu')+\mathbf{Z}^{cm}(\tau;\mu,\mu')\mathbf{L}^{sm}(\tau;\mu')]\,d\mu'+\frac{\varpi(\tau)}{4\pi}\mathbf{Z}^{sm}(\tau;\mu,\mu_0)\mathbf{F_0}\exp(-\tau/\mu_0) \tag{7}$$

Using the Gaussian-quadrature method, Eqs. (5)–(7) can be rewritten as

$$\mu\frac{d\mathbf{L}^0(\tau;\mu_i)}{d\tau}=-\mathbf{L}^0(\tau;\mu_i)+\sum_{\substack{j=-N\\ j\neq0}}^{N}\frac{\varpi(\tau)}{2}\mathbf{Z}^0(\tau;\mu_i,\mu_j)\mathbf{L}^0(\tau;\mu_j)w_j+\frac{\varpi(\tau)}{4\pi}\mathbf{Z}^0(\tau;\mu_i,\mu_0)\mathbf{F_0}\exp(-\tau/\mu_0) \tag{8}$$

$$\mu\frac{d\mathbf{L}^{cm}(\tau;\mu_i)}{d\tau}=-\mathbf{L}^{cm}(\tau;\mu_i)+\sum_{\substack{j=-N\\ j\neq0}}^{N}\frac{\varpi(\tau)}{4}[\mathbf{Z}^{cm}(\tau;\mu_i,\mu_j)\mathbf{L}^{cm}(\tau;\mu_j)-\mathbf{Z}^{sm}(\tau;\mu_i,\mu_j)\mathbf{L}^{sm}(\tau;\mu_j)]w_j+\frac{\varpi(\tau)}{4\pi}\mathbf{Z}^{cm}(\tau;\mu_i,\mu_0)\mathbf{F_0}\exp(-\tau/\mu_0) \tag{9}$$

$$\mu\frac{d\mathbf{L}^{sm}(\tau;\mu_i)}{d\tau}=-\mathbf{L}^{sm}(\tau;\mu_i)+\sum_{\substack{j=-N\\ j\neq0}}^{N}\frac{\varpi(\tau)}{4}[\mathbf{Z}^{sm}(\tau;\mu_i,\mu_j)\mathbf{L}^{cm}(\tau;\mu_j)+\mathbf{Z}^{cm}(\tau;\mu_i,\mu_j)\mathbf{L}^{sm}(\tau;\mu_j)]w_j+\frac{\varpi(\tau)}{4\pi}\mathbf{Z}^{sm}(\tau;\mu_i,\mu_0)\mathbf{F_0}\exp(-\tau/\mu_0) \tag{10}$$

where μ_i and μ_j are the nodes of the Legendre polynomial of order $2N$, and w_j is the corresponding Gaussian-quadrature weight. Here, we define the combined Stokes vector and scattering phase matrices as

$$\mathbf{L}_m=\begin{bmatrix}\mathbf{L}^{cm}\\ \mathbf{L}^{sm}\end{bmatrix} \tag{11}$$

$$\mathbf{H}_m = \begin{bmatrix} \mathbf{Z}^{cm} & -\mathbf{Z}^{sm} \\ \mathbf{Z}^{sm} & \mathbf{Z}^{cm} \end{bmatrix} \tag{12}$$

$$\mathbf{Z}_m = \begin{bmatrix} \mathbf{Z}^{cm} \\ \mathbf{Z}^{sm} \end{bmatrix} \tag{13}$$

Then, Eqs. (9) and (10) can be rewritten as

$$\mu \frac{d\mathbf{L}_m(\tau;\mu_i)}{d\tau} = -\mathbf{L}_m(\tau;\mu_i) + \sum_{\substack{j=-N \\ j\neq 0}}^{N} \frac{\varpi(\tau)}{4}\mathbf{H}_m(\tau;\mu_i,\mu_j)\mathbf{L}_m(\tau;\mu_j)w_j + \frac{\varpi(\tau)}{4\pi}\mathbf{Z}_m(\tau;\mu_i,\mu_0)\mathbf{F_0}\exp(-\tau/\mu_0), \quad m = 1,2,\ldots,M \tag{14}$$

Eqs. (8) and (14) have a similar form, and can be rewritten in the matrix form as

$$\mathbf{N}\frac{d\mathbf{L}_m^+(\tau)}{d\tau} = -\mathbf{L}_m^+(\tau) + \frac{\varpi(\tau)}{4}(1+\delta_{(0,m)})[\mathbf{H}_m^{+\,+}(\tau)\mathbf{W}\mathbf{L}_m^+(\tau) + \mathbf{H}_m^{+\,-}(\tau)\mathbf{W}\mathbf{L}_m^-(\tau)] + \mathbf{J}_{\mathbf{0}m}^+(\tau) \tag{15}$$

$$\mathbf{N}\frac{d\mathbf{L}_m^-(\tau)}{d\tau} = \mathbf{L}_m^-(\tau) - \frac{\varpi(\tau)}{4}(1+\delta_{(0,m)})[\mathbf{H}_m^{-\,+}(\tau)\mathbf{W}\mathbf{L}_m^+(\tau) + \mathbf{H}_m^{-\,-}(\tau)\mathbf{W}\mathbf{L}_m^-(\tau)] + \mathbf{J}_{\mathbf{0}m}^-(\tau) \tag{16}$$

where superscripts "+" and "−" represent the downward and the upward; δ is the Kronecker δ; $\mathbf{J}_{\mathbf{0}m}$ is the vector of the source term corresponding to the last item of Eqs. (8) and (14); **N** and **W** are the diagonal matrices $diag[\mu_1,\mu_2,\ldots,\mu_N]$ and $diag[w_1,w_2,\ldots,w_N]$, respectively. For a very thin layer with the optical thickness of $\Delta\tau$, Eqs. (15) and (16) can be rewritten in the difference approximation form as

$$\begin{aligned}\mathbf{L}_m^+(\tau+\Delta\tau) = {} & \left[\mathbf{E} - \mathbf{N^{-1}}\Delta\tau + \frac{\varpi(\tau)\Delta\tau}{4}(1+\delta_{(0,m)})\mathbf{N^{-1}}\mathbf{H}_m^{+\,+}(\tau)\mathbf{W}\right]\mathbf{L}_m^+(\tau) \\ & + \left[\frac{\varpi(\tau)\Delta\tau}{4}(1+\delta_{(0,m)})\mathbf{N^{-1}}\mathbf{H}_m^{+\,-}(\tau)\mathbf{W}\right]\mathbf{L}_m^-(\tau+\Delta\tau) + \Delta\tau\mathbf{N^{-1}}\mathbf{J}_{\mathbf{0}m}^+(\tau+\Delta\tau)\end{aligned} \tag{17}$$

$$\mathbf{L}_m^-(\tau) = \left[\mathbf{E} - \mathbf{N^{-1}}\Delta\tau + \frac{\varpi(\tau)\Delta\tau}{4}(1+\delta_{(0,m)})\mathbf{N^{-1}}\mathbf{H}_m^{-\,-}(\tau)\mathbf{W}\right]\mathbf{L}_m^-(\tau+\Delta\tau) + \left[\frac{\varpi(\tau)\Delta\tau}{4}(1+\delta_{(0,m)})\mathbf{N^{-1}}\mathbf{H}_m^{-\,+}\mathbf{W}\right]\mathbf{L}_m^+(\tau) + \Delta\tau\mathbf{N^{-1}}\mathbf{J}_{\mathbf{0}m}^-(\tau) \tag{18}$$

Defining the following parameters as

$$\begin{cases} \mathbf{R}_m^+(\Delta\tau) = \dfrac{\varpi_0(\tau)\Delta\tau}{4}(1+\delta_{(0,m)})\mathbf{N^{-1}}\mathbf{H}_m^{-\,+}\mathbf{W} \\ \mathbf{R}_m^-(\Delta\tau) = \dfrac{\varpi_0(\tau)\Delta\tau}{4}(1+\delta_{(0,m)})\mathbf{N^{-1}}\mathbf{H}_m^{+\,-}(\tau)\mathbf{W} \\ \mathbf{T}_m^+(\Delta\tau) = \mathbf{E} - \mathbf{N^{-1}}\Delta\tau + \dfrac{\varpi_0(\tau)\Delta\tau}{4}(1+\delta_{(0,m)})\mathbf{N^{-1}}\mathbf{H}_m^{+\,+}(\tau)\mathbf{W} \\ \mathbf{T}_m^-(\Delta\tau) = \mathbf{E} - \mathbf{N^{-1}}\Delta\tau + \dfrac{\varpi_0(\tau)\Delta\tau}{4}(1+\delta_{(0,m)})\mathbf{N^{-1}}\mathbf{H}_m^{-\,-}(\tau)\mathbf{W} \\ \mathbf{J}_m^+(\tau) = \Delta\tau\mathbf{N^{-1}}\mathbf{J}_{\mathbf{0}m}^+(\tau) \\ \mathbf{J}_m^-(\tau) = \Delta\tau\mathbf{N^{-1}}\mathbf{J}_{\mathbf{0}m}^-(\tau) \end{cases} \tag{19}$$

where **R**, **T** and **J** are the reflection matrixes, the transmission matrixes and the internal radiation sources of the thin layer, respectively, Eqs. (17) and (18) can be rewritten as Eqs. (20) and (21), which are the basic equations of the adding-doubling method:

$$\mathbf{L}_m^+(\tau+\Delta\tau) = \mathbf{T}_m^+(\Delta\tau)\mathbf{L}_m^+(\tau) + \mathbf{R}_m^-(\Delta\tau)\mathbf{L}_m^-(\tau+\Delta\tau) + \mathbf{J}_m^+(\tau+\Delta\tau) \tag{20}$$

$$\mathbf{L}_m^-(\tau) = \mathbf{T}_m^-(\Delta\tau)\mathbf{L}_m^-(\tau+\Delta\tau) + \mathbf{R}_m^+(\Delta\tau)\mathbf{L}_m^+(\tau) + \mathbf{J}_m^-(\tau) \tag{21}$$

The schematic diagram of the adding-doubling method is shown in Fig. 1; there are two adjacent layers, named L_{01} and L_{12}. Using Eqs. (20) and (21), there are relationships for layer L_{01} as (here we omit the index denoting the order of Fourier series)

$$\mathbf{L_1^+} = \mathbf{T_{01}}\mathbf{L_0^+} + \mathbf{R_{10}}\mathbf{L_1^-} + \mathbf{J_{01}^+} \tag{22}$$

$$\mathbf{L_0^-} = \mathbf{R_{01}}\mathbf{L_0^+} + \mathbf{T_{10}}\mathbf{L_1^-} + \mathbf{J_{10}^-} \tag{23}$$

where $\mathbf{T_{01}}$ and $\mathbf{T_{10}}$ quantify the transmission of the downward radiance and the upward radiance, respectively; $\mathbf{R_{01}}$ and $\mathbf{R_{10}}$ are the reflection of the downward radiance and the upward radiance, respectively; $\mathbf{J_{10}}^-$ is the contribution of the internal radiation sources to the upward radiance at the interface 0, and $\mathbf{J_{01}}^+$ is the contribution of the internal radiation sources to the downward radiance at the interface 1. For layer L_{12}, there are similar relationships as

$$\mathbf{L_2^+} = \mathbf{T_{12}}\mathbf{L_1^+} + \mathbf{R_{21}}\mathbf{L_2^-} + \mathbf{J_{12}^+} \tag{24}$$

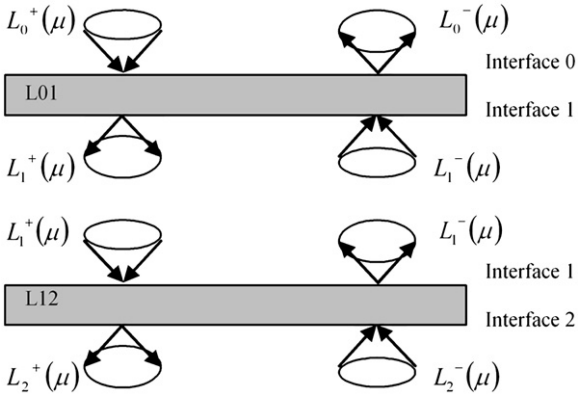

Fig. 1. Schematic diagram of the adding–doubling method. L_{01} and L_{12} are the two adjacent layers with the incident radiances $\mathbf{L_0}^+$ and $\mathbf{L_2}^-$ on the upper interface 0 and lower interface 2, respectively.

$$\mathbf{L_1^-} = \mathbf{R_{12}L_1^+} + \mathbf{T_{21}L_2^-} + \mathbf{J_{21}^-} \tag{25}$$

Combining layer L_{01} with layer L_{12}, we obtain the relationships for the combined layer L_{02} as follos:

$$\mathbf{L_2^+} = \mathbf{T_{02}L_0^+} + \mathbf{R_{20}L_2^-} + \mathbf{J_{02}^+} \tag{26}$$

$$\mathbf{L_0^-} = \mathbf{T_{20}L_2^-} + \mathbf{R_{02}L_0^+} + \mathbf{J_{20}^-} \tag{27}$$

With Eqs. (22)–(27), the radiance distribution at the internal interface 1 can be expressed as

$$\mathbf{L_1^-} = (\mathbf{E}-\mathbf{R_{12}R_{10}})^{-1}(\mathbf{R_{12}T_{01}L_0^+} + \mathbf{T_{21}L_2^-} + \mathbf{J_{21}^-} + \mathbf{R_{12}J_{01}^+}) \tag{28}$$

$$\mathbf{L_1^+} = (\mathbf{E}-\mathbf{R_{10}R_{12}})^{-1}(\mathbf{R_{10}T_{21}L_2^-} + \mathbf{T_{01}L_0^+} + \mathbf{J_{01}^+} + \mathbf{R_{10}J_{21}^-}) \tag{29}$$

Substituting Eq. (29) into Eq. (24), we have

$$\mathbf{L_2^+} = [\mathbf{T_{12}}(\mathbf{E}-\mathbf{R_{10}R_{12}})^{-1}\mathbf{T_{01}}]\mathbf{L_0^+} + [\mathbf{T_{12}}(\mathbf{E}-\mathbf{R_{10}R_{12}})^{-1}\mathbf{R_{10}T_{21}} + \mathbf{R_{21}}]\mathbf{L_2^-} + \mathbf{J_{12}^+} + \mathbf{T_{12}}(\mathbf{E}-\mathbf{R_{10}R_{12}})^{-1}(\mathbf{J_{01}^+} + \mathbf{R_{10}J_{21}^-}) \tag{30}$$

Comparing Eq. (26) with Eq. (30), we have relationships of the transmission and reflection matrices, and the internal radiation sources for the downward radiance of combined layer L_{02} as

$$\mathbf{T_{02}} = \mathbf{T_{12}}(\mathbf{E}-\mathbf{R_{10}R_{12}})^{-1}\mathbf{T_{01}} \tag{31}$$

$$\mathbf{R_{20}} = \mathbf{T_{12}}(\mathbf{E}-\mathbf{R_{10}R_{12}})^{-1}\mathbf{R_{10}T_{21}} + \mathbf{R_{21}} \tag{32}$$

$$\mathbf{J_{02}^+} = \mathbf{J_{12}^+} + \mathbf{T_{12}}(\mathbf{E}-\mathbf{R_{10}R_{12}})^{-1}(\mathbf{J_{01}^+} + \mathbf{R_{10}J_{21}^-}) \tag{33}$$

Similarly, we have relationships of the transmission and reflection matrices, and the internal radiation sources for the upward radiance of the combined layer L_{02} as

$$\mathbf{T_{20}} = \mathbf{T_{10}}(\mathbf{E}-\mathbf{R_{12}R_{10}})^{-1}\mathbf{T_{21}} \tag{34}$$

$$\mathbf{R_{02}} = \mathbf{T_{10}}(\mathbf{E}-\mathbf{R_{12}R_{10}})^{-1}\mathbf{R_{12}T_{01}} + \mathbf{R_{01}} \tag{35}$$

$$\mathbf{J_{20}^-} = \mathbf{J_{10}^-} + \mathbf{T_{10}}(\mathbf{E}-\mathbf{R_{12}R_{10}})^{-1}(\mathbf{J_{21}^-} + \mathbf{R_{12}J_{01}^+}) \tag{36}$$

Therefore, if the reflection matrices, transmission matrices and the internal radiation sources of the layers L_{01} and L_{12} are known, then these properties of the combined layer L_{02} can be derived from Eqs. (31) to (36), and the radiance distribution at the internal interface can be derived from Eqs. (28) and (29). For practical application, the vertical profile of the medium is separated by several homogeneous layers, and each layer must be divided by a number of optically very thin layers whose reflection matrices, transmission matrices and the internal radiation sources can be calculated by Eq. (19). Using Eqs. (31)–(36) repeatedly, these very thin layers can be combined into a whole layer.

2.3. Coupling of atmosphere and ocean radiative transfer

For the radiative transfer in the simple atmosphere or ocean medium, the Gaussian-quadrature points and weights are the same in all thin sub-layers, but it is not the case for the coupled ocean–atmosphere medium because of the refraction at the interface of the atmosphere and ocean. For the flat sea-surface, the incident radiance with the zenith angle ranging from 0° to 90° in the atmosphere transmits into the ocean in a cone with the maximum zenith angle less than the critical angle ($\theta_c \approx 48.3^\circ$). Therefore, the number of Gaussian-quadrature points in the ocean must be larger than the number in the

atmosphere. Generally, there are two different underwater quadrature points methods, named the coupling method and the decoupling method. The coupling method uses two sets of quadrature points, one corresponds to the refracted directions of the quadrature points in the atmosphere and the other covers the region outside the Fresnel cone [29]. The decoupling method selects the quadrature points which are not related by the refracted directions of the quadrature points in the atmosphere [37]. PCOART uses the coupling method, and the number of Gaussian-quadrature points in the ocean is set to be two times than that in the atmosphere. Here, we consider a "Gauss-Lobatto-like" quadrature problem for a function in the ocean, which can be separated into two parts as

$$\int_0^1 f(\mu^*)\,d\mu^* = \int_0^{\mu_c} f(\mu^*)\,d\mu^* + \int_{\mu_c}^1 f(\mu^*)\,d\mu^* \tag{37}$$

where μ^* is the cosine of the zenith angle in the ocean, and $\mu_c=\cos(\theta_c)$.

(1) For the first part (outside the Fresnel cone), we define $\mu^*=\mu_c\mu$, and then we have

$$\int_0^{\mu_c} f(\mu^*)\,d\mu^* = \int_0^1 f(\mu)d(\mu_c\mu) = \mu_c\int_0^1 f(\mu)d(\mu) = \sum_{i=1}^{N} f(\mu_i)(\mu_c w_i) \tag{38}$$

where μ_i and w_i are the quadrature points and weights in the atmosphere; N is the number of the Gaussian-quadrature points in the atmosphere. Therefore, for the region outside the Fresnel cone, the quadrature points and weights in the ocean are as follows:

$$\begin{cases} \mu_i^* = \mu_c\mu_i, & i=1,2,\ldots,N \\ w_i^* = \mu_c w_i, & i=1,2,\ldots,N \end{cases} \tag{39}$$

(2) For the second part (inside the Fresnel cone), according to Snell's law, the quadrature points in the ocean are

$$\mu_i^* = \sqrt{1-(1-\mu_i^2)/n_w^2}, \quad i=1,2,\ldots,N \tag{40}$$

where the refractive index of the sea water n_w is 1.34. Then, we have

$$\int_{\mu_c}^1 f(\mu^*)\,d\mu^* = \int_0^1 f(\mu)\frac{\mu}{n_w^2\mu^*}\,d\mu = \sum_{i=1}^{N} f(\mu_i)\left(\frac{\mu}{n_w^2\mu^*}w_i\right) \tag{41}$$

Therefore, the weights in the ocean are

$$w_i^* = \frac{\mu_i}{\mu_i^*}\cdot\frac{w_i}{n_w^2}, \quad i=1,2,\ldots,N \tag{42}$$

To ensure the energy conservation, the sum of the weights in the two parts should be unit. As we can see the sum of the weights in the first part is μ_c, and the sum of the weights in the second part is $1-\mu_c$ as

$$\sum_{i=1}^{N} w_i^* = \sum_{i=1}^{N}\frac{\mu_i}{\mu_i^*}\frac{w_i}{n_w^2} = \int_0^1\frac{\mu_i}{\mu_i^*}\frac{d\mu_i}{n_w^2} = \int_{\mu_c}^1\frac{d\mu_i^* 2}{2\mu_i^*} = 1-\mu_c \tag{43}$$

Compared with the simple atmosphere or ocean medium, the key layer $L(n_{oa})$ to deal with the radiative transfer process at the interface of the atmosphere and ocean must be added to couple the ocean and atmosphere. The schematic diagram of layers in the coupled ocean–atmosphere system is shown in Fig. 2; for the adjacent layers in the atmosphere or the ocean, such as layers $L(n-2)$ and $L(n-1)$, we can use Eqs. (31)–(36) directly. However, when adding the adjacent layers $L(n-1)$ and $L(n)$, we must add the layers $L(n-1)$ and $L(n_{oa})$ first to get the combined layer $L(combine)$, before adding the

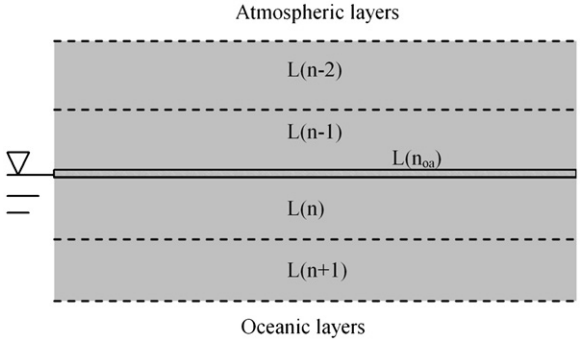

Fig. 2. Schematic diagram of layers in the coupled ocean–atmosphere system. $L(n-2)$ and $L(n-1)$ are the two adjacent layers in the atmospheric; $L(n)$ and $L(n+1)$ are the two adjacent layers in the ocean; $L(n_{oa})$ is the interface layer of the atmosphere and ocean.

layers $L(combine)$ and $L(n)$. In this processing, the key is to get the reflection matrices, transmission matrices and the internal radiation sources of the ocean–atmosphere interface layer, which will be described in detail in Section 2.4. Meanwhile, another boundary interface that should be considered is the ocean bottom, which can be taken as a Lambert reflection surface with fully depolarized reflected radiance. Detailed derivations of the reflection matrices, transmission matrices and the internal radiation sources of the ocean bottom were given in [38] and will not be repeated here.

2.4. The reflection–transmission matrices and internal radiation sources for rough sea surface

A rough sea surface can be approximated by small planar facets, and the probability density distribution of the facets' slope can be well approximated by a two-dimensional Gaussian probability density distribution [42]. In the presented version of PCOART, the wind direction is not considered, and the sea surface facets slope distribution is [26]

$$p(\mathbf{e_n}) = p(|\mu_n|) = \frac{1}{\pi\sigma^2|\mu_n^3|}\exp\left(-\frac{1}{\sigma^2}\frac{1-|\mu_n|^2}{|\mu_n|^2}\right) \tag{44}$$

where $\mathbf{e_n}$ is the normal direction vector of the facet; μ_n is the cosine of zenith angle of the vector $\mathbf{e_n}$; σ^2 is the variance, which depends on the horizontal wind speed V (in m/s) at a height of 10 m above the sea surface as [42]

$$\sigma^2 = 0.003 + 0.00512V \tag{45}$$

$p(\mathbf{e_n})$ is subject to the following normalization condition:

$$\int_{-\pi}^{\pi}\int_{0}^{1} p(\mathbf{e_n})\, d\mu_n\, d\phi_n = 1 \tag{46}$$

Here, we assume the reflection and transmission matrices of the facet are $\mathbf{r}(\pm\mu_i,\phi_i\rightarrow\mp\mu_r,\phi_r)$ and $\mathbf{t}(\pm\mu_i,\phi_i\rightarrow\pm\mu_t,\phi_t)$, respectively. μ_i, μ_r and μ_t are the cosine of zenith angles of the incident, reflection and transmission radiance vectors, respectively; ϕ_i, ϕ_r and ϕ_t are the corresponding azimuth angles. The geometries of the incident, reflection and transmission radiance vectors must obey the Fresnel law relative to the facets. It is worth noting that the cosine of zenith angle is positive for the downward radiance vector, and here for convenience, we take the values of μ_i, μ_r and μ_t as positive. Then, the total reflection and transmission radiance vectors are the sum of the reflection and transmission of all facets as

$$\begin{cases} \mathbf{L_r}(\mp\mu_r,\phi_r) = \int_0^{2\pi}\int_0^1 \mathbf{r}(\pm\mu,\phi\rightarrow\mp\mu_r,\phi_r)\mathbf{L_i}(\pm\mu,\phi)d\mu\, d\phi \\ \mathbf{L_t}(\pm\mu_t,\phi_t) = \int_0^{2\pi}\int_0^1 \mathbf{t}(\pm\mu,\phi\rightarrow\pm\mu_t,\phi_t)\mathbf{L_i}(\pm\mu,\phi)d\mu\, d\phi \end{cases} \tag{47}$$

Expanding $\mathbf{L_r}$, $\mathbf{L_t}$, $\mathbf{L_i}$, $\mathbf{r}$ and $\mathbf{t}$ into the Fourier series as

$$\begin{cases} \mathbf{L_r}(\mu_r,\phi_r) = \mathbf{L_r^0}(\mu_r) + \sum_{m=1}^{M}[\mathbf{L_r^{cm}}(\mu_r)\cos m(\phi_r-\phi_0) + \mathbf{L_r^{sm}}(\mu_r)\sin m(\phi_r-\phi_0)] \\ \mathbf{L_t}(\mu_t,\phi_t) = \mathbf{L_t^0}(\mu_t) + \sum_{m=1}^{M}[\mathbf{L_t^{cm}}(\mu_t)\cos m(\phi_t-\phi_0) + \mathbf{L_t^{sm}}(\mu_t)\sin m(\phi_t-\phi_0)] \\ \mathbf{L_i}(\mu,\phi) = \mathbf{L_i^0}(\mu_t) + \sum_{m=1}^{M}[\mathbf{L_i^{cm}}(\mu)\cos m(\phi-\phi_0) + \mathbf{L_i^{sm}}(\mu)\sin m(\phi-\phi_0)] \\ \mathbf{r}(\mu,\phi\rightarrow\mu_r,\phi_r) = \mathbf{r}^0(\mu_r,\mu) + \sum_{m=1}^{M}[\mathbf{r}^{cm}(\mu_r,\mu)\cos m(\phi-\phi_r) + \mathbf{r}^{sm}(\mu_r,\mu)\sin m(\phi-\phi_r)] \\ \mathbf{t}(\mu,\phi\rightarrow\mu_t,\phi_t) = \mathbf{t}^0(\mu_t,\mu) + \sum_{m=1}^{M}[\mathbf{t}^{cm}(\mu_t,\mu)\cos m(\phi-\phi_t) + \mathbf{t}^{sm}(\mu_t,\mu)\sin m(\phi-\phi_t)] \end{cases} \tag{48}$$

Substituting Eq. (48) into Eq. (47), and using the orthogonal property of sine and cosine functions, we get the following equations:

$$\begin{cases} \mathbf{L_r^{cm}}(\mp\mu_r) = (1+\delta_{(0,m)})\pi\int_0^1[\mathbf{r}^{cm}(\mp\mu_r,\pm\mu)\mathbf{L_i^{cm}}(\pm\mu) - \mathbf{r}^{sm}(\mp\mu_r,\pm\mu)\mathbf{L_i^{sm}}(\pm\mu)]\, d\mu, & m=0,\ldots,M \\ \mathbf{L_r^{sm}}(\mp\mu_r) = \pi\int_0^1[\mathbf{r}^{sm}(\mp\mu_r,\pm\mu)\mathbf{L_i^{cm}}(\pm\mu) + \mathbf{r}^{cm}(\mp\mu_r,\pm\mu)\mathbf{L_i^{sm}}(\pm\mu)]\, d\mu, & m=1,\ldots,M \end{cases} \tag{49}$$

$$\begin{cases} \mathbf{L_t^{cm}}(\pm\mu_t) = (1+\delta_{(0,m)})\pi\int_0^1[\mathbf{t}^{cm}(\pm\mu_t,\pm\mu)\mathbf{L_i^{cm}}(\pm\mu) - \mathbf{t}^{sm}(\pm\mu_t,\pm\mu)\mathbf{L_i^{sm}}(\pm\mu)]\, d\mu, & m=0,\ldots,M \\ \mathbf{L_t^{sm}}(\pm\mu_t) = \pi\int_0^1[\mathbf{t}^{sm}(\pm\mu_t,\pm\mu)\mathbf{L_i^{cm}}(\pm\mu) + \mathbf{t}^{cm}(\pm\mu_t,\pm\mu)\mathbf{L_i^{sm}}(\pm\mu)]\, d\mu, & m=1,\ldots,M \end{cases} \tag{50}$$

Using the Gaussian-quadrature method, Eqs. (49) and (50) can be rewritten as

$$\begin{cases} \mathbf{L}_{\mathbf{r}}^{cm}(\mp\mu_i)=(1+\delta_{(0,m)})\pi\sum_{j=1}^{N}[\mathbf{r}^{cm}(\mp\mu_i,\pm\mu_j)\mathbf{L}_{\mathbf{i}}^{cm}(\pm\mu_j)-\mathbf{r}^{sm}(\mp\mu_i,\pm\mu_j)\mathbf{L}_{\mathbf{i}}^{sm}(\pm\mu_j)]w_j, & m=0,\ldots,M \\ \mathbf{L}_{\mathbf{r}}^{sm}(\mp\mu_i)=\pi\sum_{j=1}^{N}[\mathbf{r}^{sm}(\mp\mu_i,\pm\mu_j)\mathbf{L}_{\mathbf{i}}^{cm}(\pm\mu_j)+\mathbf{r}^{cm}(\mp\mu_i,\pm\mu_j)\mathbf{L}_{\mathbf{i}}^{sm}(\pm\mu_j)]w_j, & m=1,\ldots,M \end{cases} \tag{51}$$

$$\begin{cases} \mathbf{L}_{\mathbf{t}}^{cm}(\pm\mu_i)=(1+\delta_{(0,m)})\pi\sum_{j=1}^{N}[\mathbf{t}^{cm}(\pm\mu_i,\pm\mu_j)\mathbf{L}_{\mathbf{i}}^{cm}(\pm\mu_j)-\mathbf{t}^{sm}(\pm\mu_i,\pm\mu_j)\mathbf{L}_{\mathbf{i}}^{sm}(\pm\mu_j)]w_j, & m=0,\ldots,M \\ \mathbf{L}_{\mathbf{t}}^{sm}(\pm\mu_i)=\pi\sum_{j=1}^{N}[\mathbf{t}^{sm}(\pm\mu_i,\pm\mu_j)\mathbf{L}_{\mathbf{i}}^{cm}(\pm\mu_j)+\mathbf{t}^{cm}(\pm\mu_i,\pm\mu_j)\mathbf{L}_{\mathbf{i}}^{sm}(\pm\mu_j)]w_j, & m=1,\ldots,M \end{cases} \tag{52}$$

Similarly, we define the combined reflection and transmission matrices of the facet as

$$\mathbf{r}_m=\begin{bmatrix}\mathbf{r}^{cm} & -\mathbf{r}^{sm}\\ \mathbf{r}^{sm} & \mathbf{r}^{cm}\end{bmatrix} \tag{53}$$

$$\mathbf{t}_m=\begin{bmatrix}\mathbf{t}^{cm} & -\mathbf{t}^{sm}\\ \mathbf{t}^{sm} & \mathbf{t}^{cm}\end{bmatrix} \tag{54}$$

Then, Eqs. (51) and (52) can be rewritten as

$$\begin{cases} \mathbf{L}_{\mathbf{r}}^{m}(\mp\mu_i)=(1+\delta_{(0,m)})\pi\sum_{j=1}^{N}\mathbf{r}_m(\mp\mu_i,\pm\mu_j)\mathbf{L}_{\mathbf{i}}^{m}(\pm\mu_j)w_j, & m=0,\ldots,M \\ \mathbf{L}_{\mathbf{t}}^{m}(\pm\mu_i)=(1+\delta_{(0,m)})\pi\sum_{j=1}^{N}\mathbf{t}_m(\pm\mu_i,\pm\mu_j)\mathbf{L}_{\mathbf{i}}^{m}(\pm\mu_j)w_j, & m=0,\ldots,M \end{cases} \tag{55}$$

where $\mathbf{L}_{\mathbf{r}}^{m}$, $\mathbf{L}_{\mathbf{t}}^{m}$ and $\mathbf{L}_{\mathbf{i}}^{m}$ are the combined Stokes vectors. So, the reflection and transmission matrices of the ocean–atmosphere interface layer can be rewritten as

$$\begin{cases} N\times N:\mathbf{R}_{\mathbf{m}}^{-}=(1+\delta_{(0,m)})\pi\mathbf{r}_m(-\mu_i,\mu_j)w_j, & i,j=1,\ldots,N \\ 2N\times 2N:\mathbf{R}_{\mathbf{m}}^{+}=(1+\delta_{(0,m)})\pi\mathbf{r}_m(\mu_i^*,-\mu_j^*)w_j^*, & i,j=1,\ldots,2N \\ 2N\times N:\mathbf{T}_{\mathbf{m}}^{+}=(1+\delta_{(0,m)})\pi\mathbf{t}_m(\mu_i^*,\mu_j)w_j, & i=1,\ldots,2N,\quad j=1,\ldots,N \\ N\times 2N:\mathbf{T}_{\mathbf{m}}^{-}=(1+\delta_{(0,m)})\pi\mathbf{t}_m(-\mu_i,-\mu_j^*)w_j^*, & i=1,\ldots,N,\quad j=1,\ldots,2N \end{cases} \tag{56}$$

Meanwhile, because of the diffuse reflection and transmission by the rough sea surface, the internal radiation sources for the ocean–atmosphere interface layer are represented as

$$\begin{cases} N:\mathbf{J}_{\mathbf{m}}^{-}=\mathbf{r}_m(-\mu_i,\mu_0)\mathbf{F_0}e^{(-\tau_A/\mu_0)}, & i=1,\ldots,N \\ 2N:\mathbf{J}_{\mathbf{m}}^{+}=\mathbf{t}_m(-\mu_i,\mu_0)\mathbf{F_0}e^{(-\tau_A/\mu_0)}, & i=1,\ldots,2N \end{cases} \tag{57}$$

where τ_A is the optical thickness of the atmosphere layer. From Eqs. (49) and (50), it can be seen that the reflection and transmission matrices of the facet are the key to obtain the reflection and transmission matrices of the ocean–atmosphere interface layer, which we will show in detail as follows.

2.4.1. The reflection matrix of the facet

As shown in Fig. 3, $\mathbf{L_i}$ and $\mathbf{L_r}$ are the incident and reflection radiance vectors on the facet, respectively. Here, we assume the geometry of $-\mathbf{L_i}$ is (θ',ϕ'), and the relationships between (θ',ϕ') and (θ_i,ϕ_i) are represented as

$$\begin{cases} \theta'=\pi-\theta_i \\ \phi'=\phi_i-\pi \end{cases} \tag{58}$$

The incident angle on the facet is

$$\alpha=\frac{1}{2}\cos^{-1}[\cos\theta_r\cos\theta'+\sin\theta_r\sin\theta'\cos(\phi_r-\phi')] \tag{59}$$

Then, the cosine of zenith angle of the normal vector $\mathbf{e_n}$ of the facet is

$$|\mu_n|=\frac{|\cos\theta'|+|\cos\theta_r|}{2\cos 2\alpha} \tag{60}$$

Substituting Eq. (60) into Eq. (44), we get the probability of the facets, which satisfy the special geometries of the incident and reflection radiance vectors. According to the Fresnel law, we get the reflection Mueller matrix $\mathbf{F_r}(a)$ of the

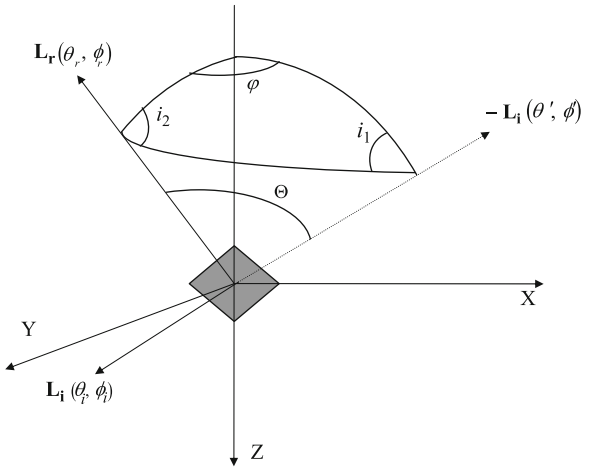

Fig. 3. Schematic diagram of the reflection of the special facet of the rough sea surface. $\mathbf{L_i}$ and $\mathbf{L_r}$ are the incident and reflection radiance vectors on the facet, respectively; $-\mathbf{L_i}$ is the inverse direction of the incident radiance vector $\mathbf{L_i}$.

facet as

$$\mathbf{F_r} = \begin{bmatrix} \rho_+ & \rho_- & 0 & 0 \\ \rho_- & \rho_+ & 0 & 0 \\ 0 & 0 & \rho_{33} & \rho_{34} \\ 0 & 0 & -\rho_{34} & \rho_{33} \end{bmatrix} \tag{61}$$

where

$$\begin{cases} \rho_\pm = \dfrac{1}{2}[|R_V|^2 \pm |R_H|^2] \\ \rho_{33} = \mathrm{Re}(R_V \bullet R_H^*) \\ \rho_{34} = -\mathrm{Im}(R_V \bullet R_H^*) \\ R_H = [\cos(\theta_i) - \sqrt{n_w^2 - 1 + \cos^2(\theta_i)}]/[\cos(\theta_i) + \sqrt{n_w^2 - 1 + \cos^2(\theta_i)}] \\ R_V = [n_w^2\cos(\theta_i) - \sqrt{n_w^2 - 1 + \cos^2(\theta_i)}]/[n_w^2\cos(\theta_i) + \sqrt{n_w^2 - 1 + \cos^2(\theta_i)}] \end{cases} \tag{62}$$

where R_H is the complex conjugate of R_H. Different from the flat sea surface, the reference planes of the incident and reflection radiance vectors are not in the same plane for the rough sea surface; therefore it needs to rotate the reference plane. According to the spherical trigonometry properties, the rotation angles are represented as

$$\begin{cases} \sin i_1 = \sin\theta_r \sin(\phi_r - \phi')/\sin 2\alpha \\ \sin i_2 = \sin\theta' \sin(\phi_r - \phi')/\sin 2\alpha \end{cases} \tag{63}$$

Using Eq. (2), we get the rotated reflection Mueller matrix for the special facet as

$$\mathbf{R_f} = \mathbf{C}(\pi - i_2)\mathbf{F_r}(\alpha)\mathbf{C}(i_1) \tag{64}$$

Furthermore, the shadowing factor should be considered, which is the probability that an individual facet is visible (i.e., not obstructed by another facet) to either the observer at (θ_r,ϕ_r) or the source at (θ_i,ϕ_i). The shadowing factor can be expressed as [23]

$$S(\theta_i,\phi_i \to \theta_r,\phi_r) = \frac{1}{1 + U(|\cos\theta_i|) + U(|\cos\theta_r|)} \tag{65}$$

where

$$U(\cos\theta) = \frac{1}{2}\left\{ \sqrt{\frac{2\sigma^2}{\pi}\frac{(1-\cos^2\theta)}{\cos^2\theta}} \exp\left[-\frac{\cos^2\theta}{2\sigma^2(1-\cos^2\theta)} \right] - erfc\left[\frac{\cos\theta}{\sigma\sqrt{2(1-\cos^2\theta)}} \right] \right\} \tag{66}$$

and the error function is given by

$$erfc(x) = \frac{2}{\sqrt{\pi}} \int_x^\infty \exp(-t^2)\, dt \tag{67}$$

Considering the cosine law for irradiance, we finally get the reflection matrix of the facet as

$$\mathbf{r}(\theta_i,\phi_i\rightarrow\theta_r,\phi_r)=\frac{1}{4|\cos\theta_r||\mu_n|}p(|\mu_n|)S(\theta_i,\phi_i\rightarrow\theta_r,\phi_r)\mathbf{R_f}(\theta_i,\phi_i\rightarrow\theta_r,\phi_r) \tag{68}$$

2.4.2. The transmission matrix of the facet

As shown in Fig. 4, $\boldsymbol{\xi_i}$ and $\boldsymbol{\xi_t}$ are the direction vectors of incident radiance vector and the transmission radiance vector, respectively. The cosine of the angle between $\boldsymbol{\xi_i}$ and $\boldsymbol{\xi_t}$ is

$$\cos\Theta=\cos\theta_i\cos\theta_t+\sin\theta_i\sin\theta_t\cos\varphi \tag{69}$$

where $\varphi(=\phi_t-\phi_i)$ is the relative azimuth angle. $\cos\Theta$ must be larger than $\sin\theta_c$ to meet Snell's law of refraction. According to Snell's law of refraction, the direction vector ($\mathbf{e_n}$) of the facet is represented as

$$\begin{cases} e_{nx}=(n_r\sin\theta_t\cos\varphi-\sin\theta_i)/\sqrt{1+n_r^2-2n_r\cos\Theta} \\ e_{ny}=n_r\sin\theta_t\sin\varphi/\sqrt{1+n_r^2-2n_r\cos\Theta} \\ e_{nz}=(n_r\cos\theta_t-\cos\theta_i)/\sqrt{1+n_r^2-2n_r\cos\Theta} \end{cases} \tag{70}$$

where n_r is the relative refraction index between the incident media and the refraction media. If the radiance incident is from the atmosphere to the ocean, the incident radiance is in the upper hemisphere of the facet until the $e_{nz}>0$ and $e_{nx}>-|\cos\theta_i|$, or $e_{nz}<0$ and $e_{nx}<|\cos\theta_i|$. If the radiance incident is from the ocean to the atmosphere, the incident radiance is in the lower hemisphere of the facet until the $e_{nz}>0$ and $e_{nx}>|\cos\theta_i|$, or $e_{nz}<0$ and $e_{nx}<-|\cos\theta_i|$. Because the cosine of zenith angle of the normal vector $\mathbf{e_n}$ of the facet is equal to e_{nz}, we can get the probability of the facet, which satisfies the special geometries of the incident and refraction radiance vectors according to Eq. (48).

The incident angle on the facet is

$$\cos\alpha=|\boldsymbol{\xi_i}\cdot\mathbf{e_n}| \tag{71}$$

According to the Fresnel law, we obtain the transmission Mueller matrix $\mathbf{F_t}(\alpha)$ as

$$\mathbf{F_t}=\frac{1}{2}\frac{n_w^2\sin(2\theta_i)\sin(2\theta_t)}{[\sin(b)\cos(a)]^2}\begin{bmatrix} 1+\cos^2(a) & 1-\cos^2(a) & 0 & 0 \\ 1-\cos^2(a) & 1+\cos^2(a) & 0 & 0 \\ 0 & 0 & 2\cos(a) & 0 \\ 0 & 0 & 0 & 2\cos(a) \end{bmatrix} \tag{72}$$

where $a=\theta_i-\theta_t$; $b=\theta_i+\theta_t$; θ_i is the incident angle α, and θ_t is the refractive angle with $\sin(\theta_t)=\sin(\theta_i)/n_w$. For the complete reflectance case, $\mathbf{F_t}=\mathbf{0}$. In the same way, it needs to rotate the reference plane. According to the spherical trigonometry properties, the rotation angles are represented as

$$\begin{cases} \sin i_1=\sin\theta_t\sin\varphi/\sin2\alpha \\ \sin i_2=\sin\theta_i\sin\varphi/\sin2\alpha \end{cases} \tag{73}$$

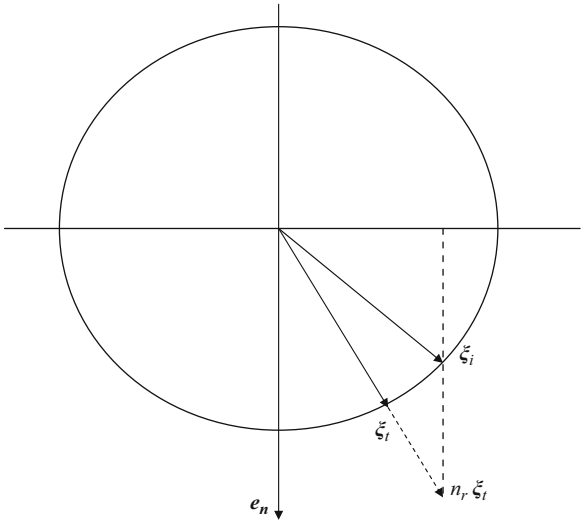

Fig. 4. Geometry of the refraction of the special facet of the rough sea surface. $\boldsymbol{\xi_i}$ and $\boldsymbol{\xi_t}$ are the direction vectors of incident radiance and the transmission radiance, respectively; $\mathbf{e_n}$ is the direction vector of the facet; n_r is the relative refraction index between the incident media and the refraction media.

Using Eq. (2), we get the rotated transmission Mueller matrix for the special facet as

$$\mathbf{T_t} = \mathbf{C}(\pi - i_2)\mathbf{F_t}(\alpha)\mathbf{C}(i_1) \tag{74}$$

Furthermore, the shadowing factor should be considered as [23]

$$S(\theta_i,\phi_i \to \theta_t,\phi_t) = \frac{1}{1+U(|\cos\theta_i|)+U(|\cos\theta_t|)} \tag{75}$$

Finally, considering the cosine law for irradiance, we get the transmission matrix of the facet as

$$\mathbf{t}(\theta_i,\phi_i \to \theta_t,\phi_t) = \frac{\cos\Theta_i \cos\Theta_t}{|\cos\theta_t||\mu_n|(\cos\Theta_i - n_r\cos\Theta_t)^2} p(|\mu_n|)S(\theta_i,\phi_i \to \theta_t,\phi_t)\mathbf{T_t}(\theta_i,\phi_i \to \theta_t,\phi_t) \tag{76}$$

where Θ_i and Θ_t are the incident and refraction angles of the facet, respectively, which can be easily derived from the direction vectors of $\boldsymbol{\xi_i}$, $\boldsymbol{\xi_t}$ and $\mathbf{e_n}$.

3. Validation and results

The validation of the PCOART is performed with several radiative transfer problems in the atmosphere and ocean, including (A) the Rayleigh atmosphere radiative transfer problem to validate the numerical accuracy of the Stokes vector calculated by the model for the rough sea-surface; (B) the standard underwater radiative transfer problems to validate the numerical accuracy of the model for both the flat and rough sea-surface; and (C) the coupled ocean–atmospheric radiative transfer problem to validate the numerical accuracy of the radiance fields in the atmosphere and ocean calculation by the model for the rough sea-surface. Finally, the polarizing remote sensing data from POLDER are used to validate the capacity of the POCART to simulate the linear polarizing radiance at the top-of-atmosphere.

3.1. Rayleigh atmosphere radiative transfer problem for rough sea surface

Rayleigh atmosphere is the idealized atmosphere that consists of only the molecules. For such atmosphere, there is no absorption in the atmosphere. Here, the case is a Rayleigh atmosphere layer above a total absorption ocean layer with a rough sea surface. For this radiative transfer problem, Gordon et al. [23,43] had solved the vector radiative transfer equation numerically using the successive-order-of-scattering method with the wind induced rough sea surface, and derived the Stokes vector at the top-of-atmosphere with the error less than 0.1%, by which the exact Rayleigh scattering look-up tables had been generated for several ocean color remote sensors, such as CZCS, SeaWiFS, MODIS, etc. Here, we use the exact Rayleigh scattering look-up tables of MODIS (hereinafter referred to as MODIS_LUT) to validate the accuracy of PCOART. In the calculation, fifty Gaussian-quadrature points are used for the atmosphere, and the Rayleigh scattering matrix is

$$\mathbf{P}(\vartheta) = \frac{3}{2}\frac{(1-\rho_0)}{(1+(\rho_0/2))}\begin{bmatrix} \frac{1}{2}\left(\frac{1+\rho_0}{1-\rho_0}+\cos^2\vartheta\right) & -\frac{1}{2}[1-\cos^2\vartheta] & 0 & 0 \\ -\frac{1}{2}[1-\cos^2\vartheta] & \frac{1}{2}[1+\cos^2\vartheta] & 0 & 0 \\ 0 & 0 & \cos\vartheta & 0 \\ 0 & 0 & 0 & \frac{(1-2\rho_0)}{(1-\rho_0)}\cos\vartheta \end{bmatrix} \tag{77}$$

where ϑ is the scattering angle; ρ_0 is the depolarization factor of the atmosphere molecule, which takes the value of ρ_0=0.0279 [44]. Because of the limited space of this paper, here we only give the validation results of 412 nm band with the solar zenith angle of 30°. The incident extraterrestrial irradiance is 1726.7 W/(m^2 μm) for the 412 nm band of MODIS. The horizontal wind speeds at 10 m height above the sea surface are 5 and 15 m/s, respectively. Figs. 5 and 6 show the comparison of the first component I of the Stokes vectors between PCOART and MODIS_LUT with the sea surface wind speeds of 5 and 15 m/s, respectively, where the relative errors are all less than 0.5% for the different observation zenith angles and relative azimuth angles. Also, the components Q and U of the Stokes vectors calculated by PCOART are consistent well with the results of MODIS_LUT, as shown in Figs. 7 and 8. The last component V of the Stokes vectors for both the PCOART and MODIS_LUT are zeros for the Rayleigh atmosphere. Therefore, the Stokes vector calculated by PCOART for the rough sea-surface is correct.

3.2. The standard underwater radiative transfer problems

The standard radiative transfer problems in ocean were well-defined by Mobley for the intercomparison of various numerical models, and the details could be found in the literature [45]. Here, five problems that cover specific aspects of the radiative transfer in the ocean are used to validate the accuracy of the current version of PCOART for both the flat and rough sea-surface, as follows:

(1) an unrealistically simple problem,
(2) a base problem using realistic inherent optical properties for the ocean,

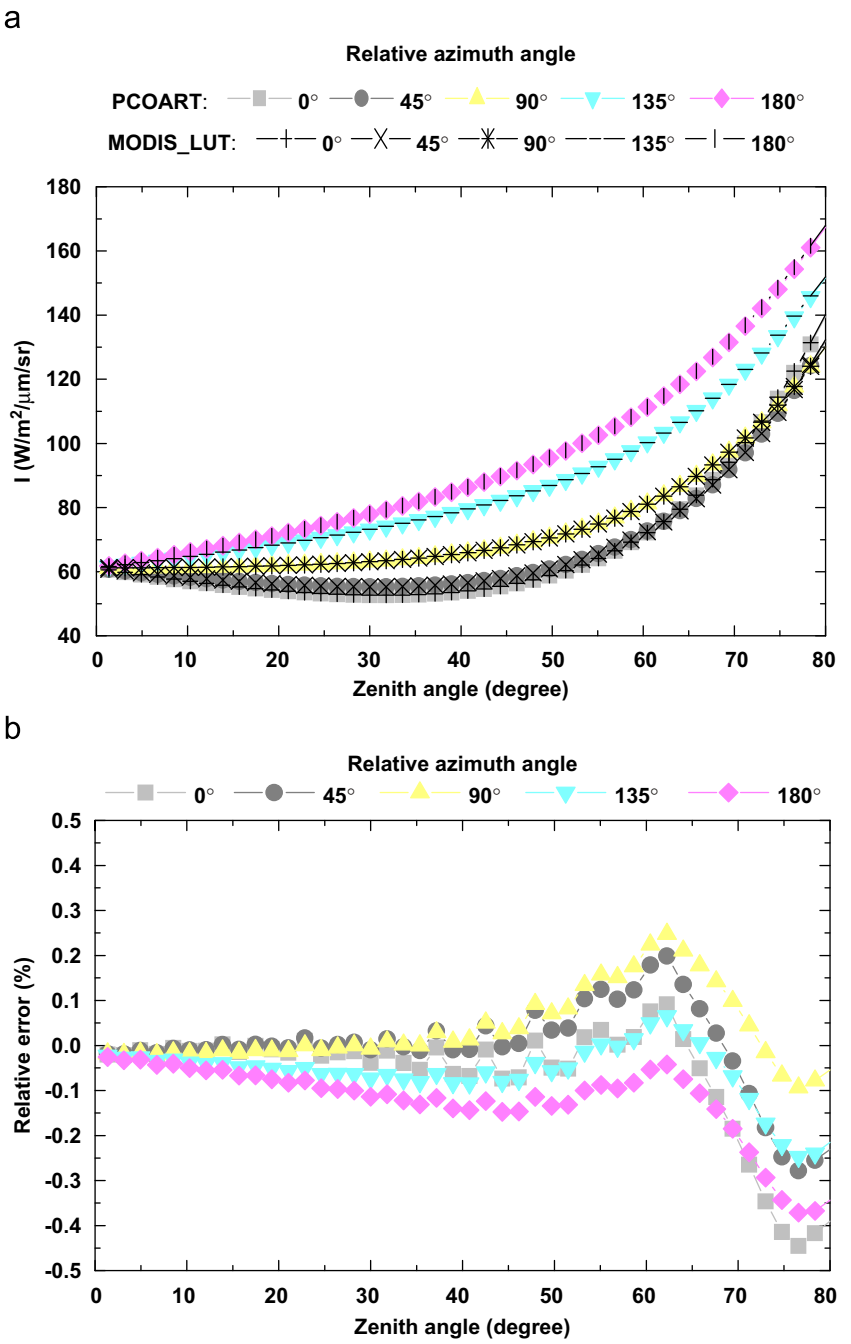

Fig. 5. Comparison of component *I* of Stokes vectors between PCOART and MODIS_LUT for different observation zenith angles and relative azimuth angles with sea surface wind speed of 5 m/s, (a) values of *I*; (b) relative errors.

(3) the base problem but with stratified water,
(4) the base problem but with a finite depth bottom, and
(5) the base problem but with a rough sea surface.

In each of these problems, the water is taken to be horizontally homogeneous with the refractive index of 1.34. The depth from the sea surface is specified by either the no dimensional optical depth τ or by the geometric depth z in meters. The first four problems assume that: (a) sea surface is flat; (b) there is no atmosphere, i.e. the sky is black; (c) the solar zenith angle is 60°; (d) the incident solar irradiance is 1.0 mW/(cm^2 μm) with E_d=0.5 mW/(cm^2 μm) for a solar zenith angle

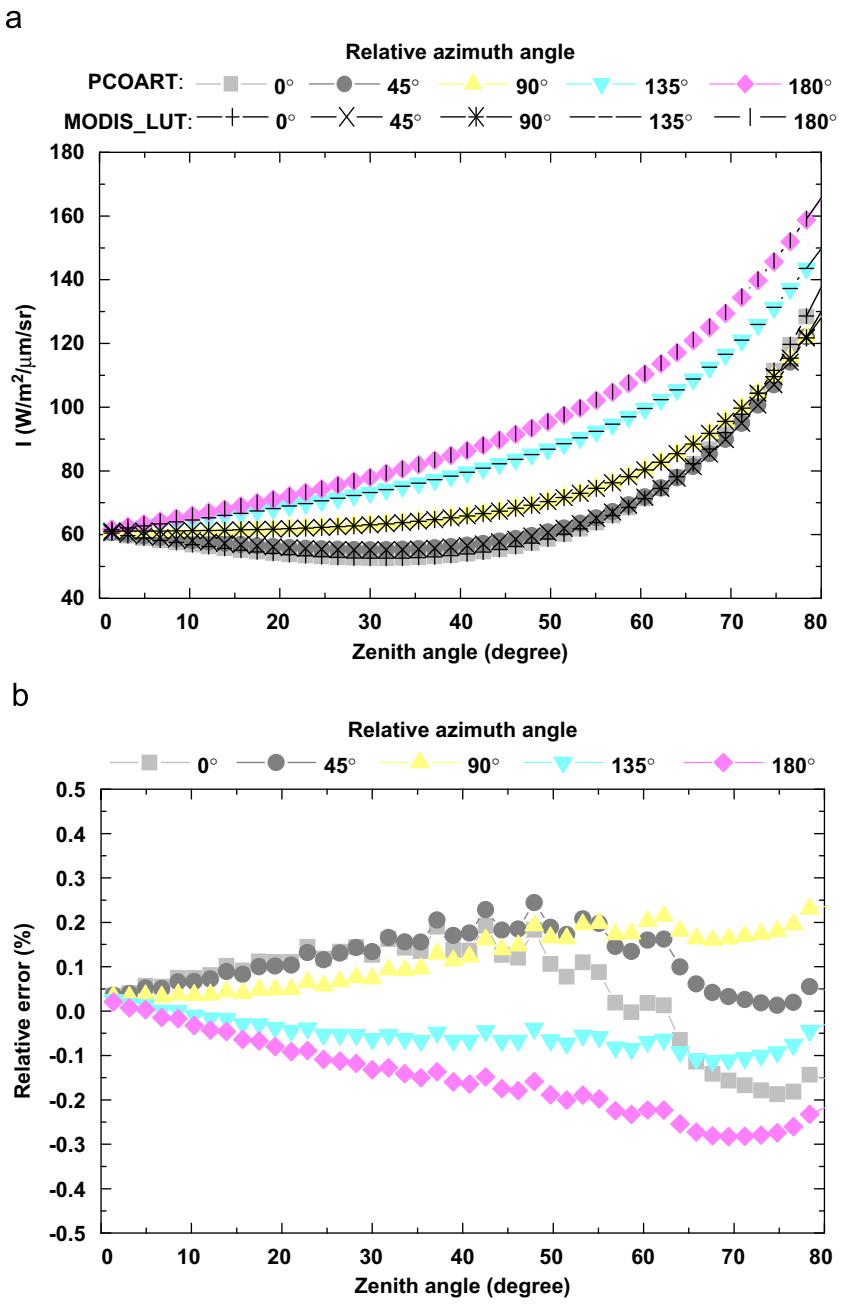

Fig. 6. Comparison of component *I* of Stokes vectors between PCOART and MODIS_LUT for different observation zenith angles and relative azimuth angles with sea surface wind speed of 15 m/s. (a) Values of *I*; (b) relative errors.

of 60°, and (e) there is no inelastic scattering or other source of light within the ocean. The first four problems were already validated by our previous version of PCOART for flat sea surface [24], and will not be repeated here. The results showed good agreements between the PCOART simulations and the average values given by Mobley et al. [45] (hereinafter referred to as AVM) for both the highly scattering and absorbing cases, which proved that PCOART could exactly predict the underwater radiance fields for the sharp forward scattering, stratified and finite depth ocean cases.

The last problem is similar to problem 2 but with rough sea surface at the solar zenith angle of 80°. The Petzold phase function [46] is used instead of the simple Rayleigh scattering phase function with the single scattering albedo (ω_0) of 0.9. In the natural water, even very low concentrations of suspended particle matter can cause sharp forward scattering. Therefore, dealing with the sharp forward scattering phase function is important for the realistic underwater radiative transfer simulation. In PCOART, the Delta-M method [47] is used to deal with the sharp forward scattering phase function.

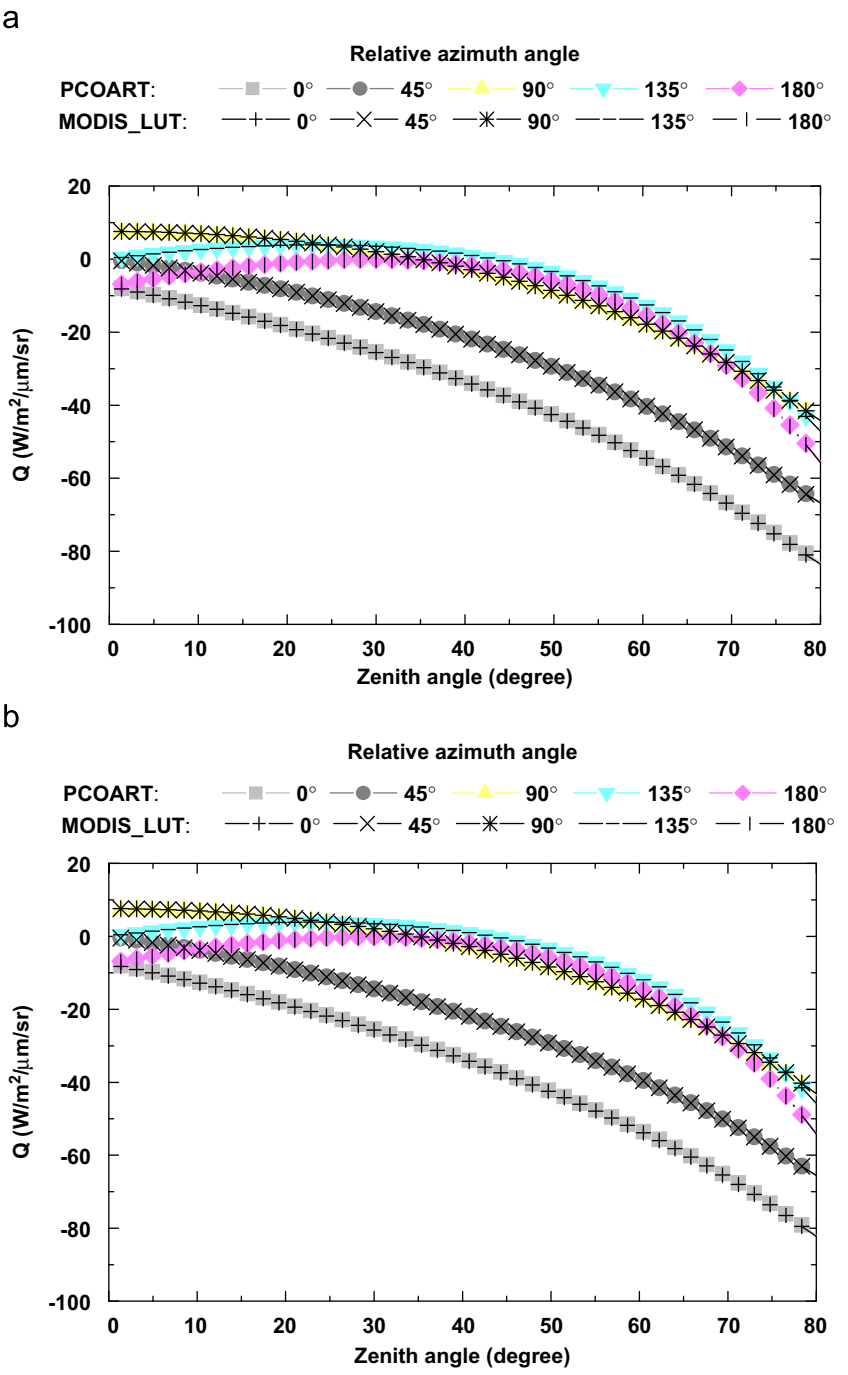

Fig. 7. Comparison of component Q of Stokes vectors between PCOART and MODIS_LUT for different observation zenith angles and relative azimuth angles. (a) Sea surface wind speed of 5 m/s; (b) sea surface wind speed of 15 m/s.

The detail derivation of the Delta-M method and the extension method for polarized light were described in the literature [31]. As shown in Fig. 9, the Delta-M truncated Petzold phase function is much smoother than the original sharp forward scattering function. In the simulation, the atmosphere–ocean system is discretized into one atmospheric layer and one oceanic layer. The atmospheric layer is completely clear with no extinction, and the depth of the oceanic layer is infinite. The simulations were performed using ten Gaussian-quadrature points in atmosphere and twenty Gaussian-quadrature points in ocean with the sea surface wind speed of 7.23 m/s. Table 1 shows the comparison results of the downward irradiance (E_d), the upward scalar irradiance (E_{ou}) and the upward nadir radiance (L_u) at three optical depths calculated by

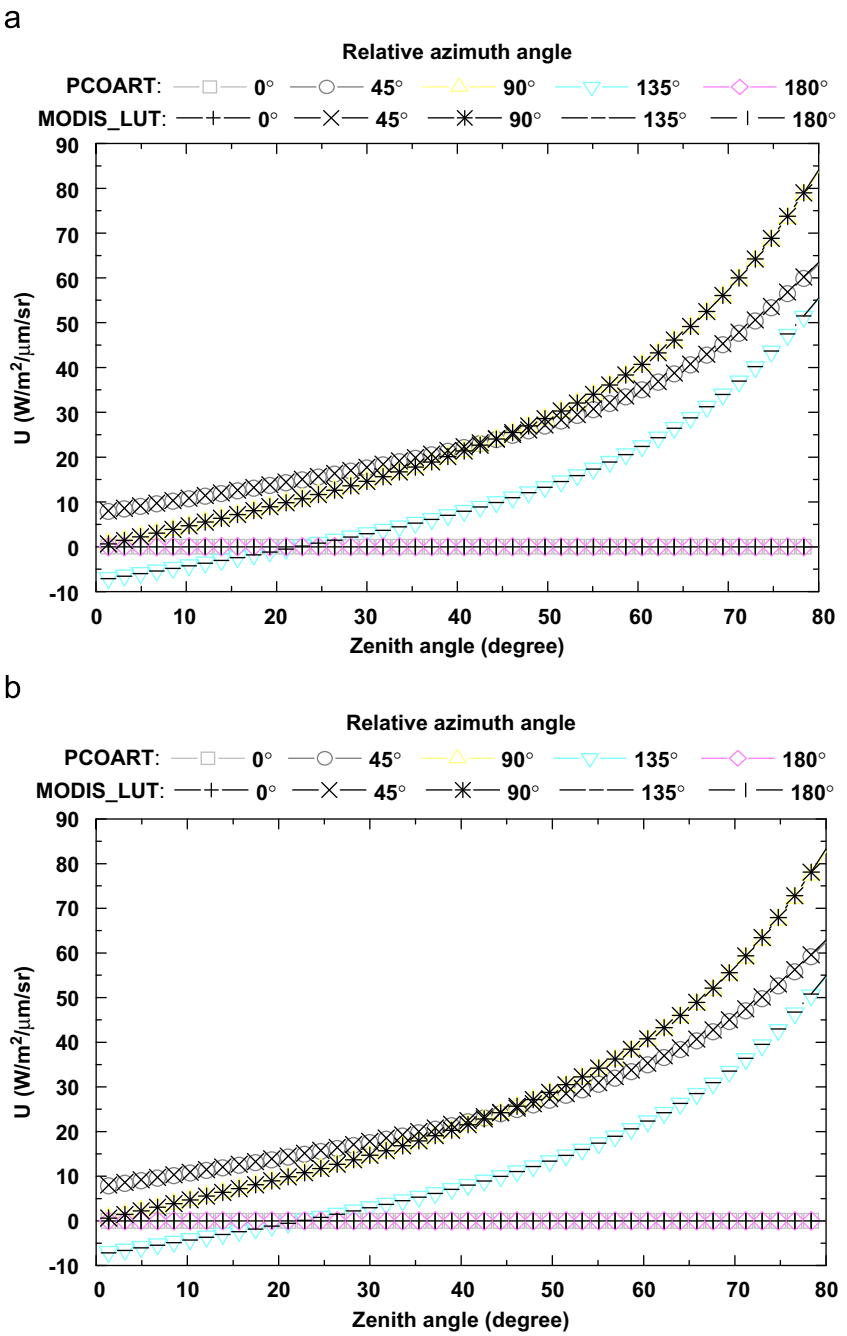

Fig. 8. Comparison of component *U* of Stokes vectors between PCOART and MODIS_LUT for different observation zenith angles and relative azimuth angles. (a) Sea surface wind speed of 5 m/s; (b) sea surface wind speed of 15 m/s.

PCOART with the AVM. There is also good agreement between the PCOART results and the Mobley-derived average values for the underwater radiative transfer problem with rough sea surface.

3.3. The coupled ocean–atmosphere radiative transfer problem for rough sea surface

To the best of the authors' knowledge, there is no standard value of the vector radiative transfer problem of coupled ocean–atmosphere system for rough sea surface. Here, we use the scalar radiative transfer code named coupled ocean atmosphere radiative transfer (COART) model to validate the numerical accuracy of the radiance fields in the atmosphere and ocean calculation by PCOART for rough sea-surface. COART is the scalar radiative transfer code using the discrete

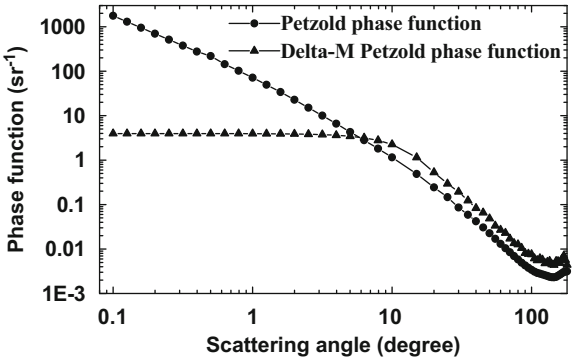

Fig. 9. Comparison of the original Petzold phase function and the Delta-M truncated function.

Table 1
Intercomparison of PCOART predictions with average values and standard deviations by Mobley et al. [45] for problem 5.

τ	E_d [mW/(cm^2 μm)]		$\boldsymbol{E}_{ou}$ [mW/(cm^2 μm)]		$\boldsymbol{L}_{u}$ [mW/(cm^2 μm sr)]	
	PCOART	AVM	PCOART	AVM	PCOART	AVM
1	1.147E−1	1.14 ± 0.02E−1	3.534E−2	3.55 ± 0.08E−2	2.040E−3	2.09 ± 0.07E−3
5	4.392E−2	4.33 ± 0.04E−2	1.232E−2	1.22 ± 0.04E−2	7.458E−4	7.63 ± 0.28E−4
10	1.505E−2	1.48 ± 0.02E−2	3.696E−3	3.65 ± 0.08E−3	2.491E−4	2.49 ± 0.07E−4

ordinates method for rough sea surface, based on the Coupled DIScrete Ordinate Radiative Transfer (Coupled DISTORT or CDISORT) code developed from DISORT, which is the public distributed software for radiative transfer by NASA [29]. The same radiative transfer problem of coupled ocean–atmosphere system with rough sea-surface was calculated both by PCOART and by COART with the following conditions:

(1) The United Sates Standard Atmospheric Model (US62) with none aerosol, or Rayleigh atmosphere;
(2) rough sea surface with the horizontal wind speeds 5 and 15 m/s at 10 m height above the sea surface, respectively;
(3) infinite water depth;
(4) vertical uniform chlorophyll concentration of 1.0 μg/l; and
(5) Petzold phase function [46].

For the no-absorption Rayleigh atmosphere, the vertical profile of the atmosphere molecule can affect the radiance distribution in the atmosphere; however, it does not affect the upward radiance at the top-of-atmosphere and the downward radiance at the sea surface. If we consider the radiance at the top-of-atmosphere, the Rayleigh atmosphere can be taken as a uniform layer. In the simulation by PCAORT, the atmosphere–ocean system is discretized into one Rayleigh atmosphere layer and one oceanic layer. Because of the limitation of the space, here we only give the validation results of 412 nm with a solar zenith angle of 30°. The simulations were performed using ten Gaussian-quadrature points in atmosphere and twenty Gaussian-quadrature points in ocean for PCOART. Fig. 10 shows the comparison results of the radiance fields at the top-of-atmosphere, just above sea surface and at 5 m depth underwater between PCOART and COART with the horizontal wind speeds at 10 m height above the sea surface of 5 m/s. Radiances with zenith angle between 0° and 90° represent the upward radiances, and radiances with zenith angle between 90° and 180° represent the downward radiances. It can be seen that there are good agreements between PCOART and COART results for the radiance fields at the top-of-atmosphere and just above sea surface. For the radiance field at 5 m depth underwater, there is a large difference of the downward radiance around the solar refraction direction where PCOART results are much smaller than COART. As we know, the Delta-M method will artificially enhance the direct-beam component of flux at the expense of the diffuse component, but the sum of the two will be computed accurately [48]. Therefore, the simulated downward radiance near the solar direction (aureole) will be reduced using the Delta-M method. To remedy this limitation, COART uses the Nakajima and Tanaka algorithms [49] to correct the radiance near the solar direction, which use the "correct" single/double scattering radiance to replace the "wrong" single/double scattering radiance calculated by COART. So, COART can simulate the radiance near the solar direction more accurately. However, this correction has not been adopted in the current version of PCOART. Another reason is that twenty Gaussian-quadrature points in ocean are too little to express the radiation of the aureole region. Generally, the larger the number of the Gaussian-quadrature point, the more accurate the radiance near the aureole region. However, the computation burden grows as the cube of the number of the

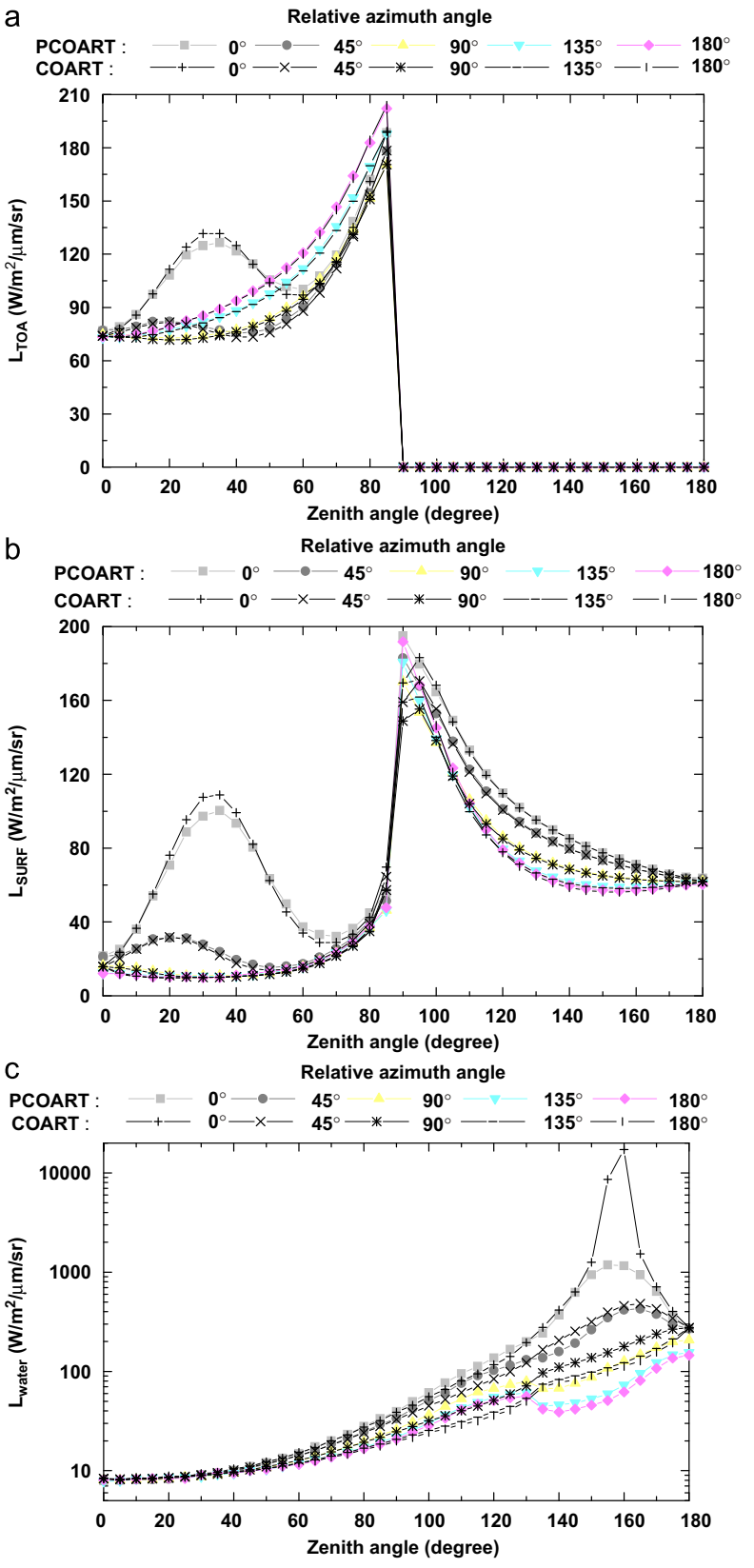

Fig. 10. Comparison of the 412 nm radiance fields at top-of-atmosphere, just above sea surface and 5 m depth underwater between PCOART and COART with the horizontal wind speeds at a height of 10 m above the sea surface of 5 m/s. (a) Top-of-atmosphere, (b) just above sea surface, (c) 5 m depth underwater.

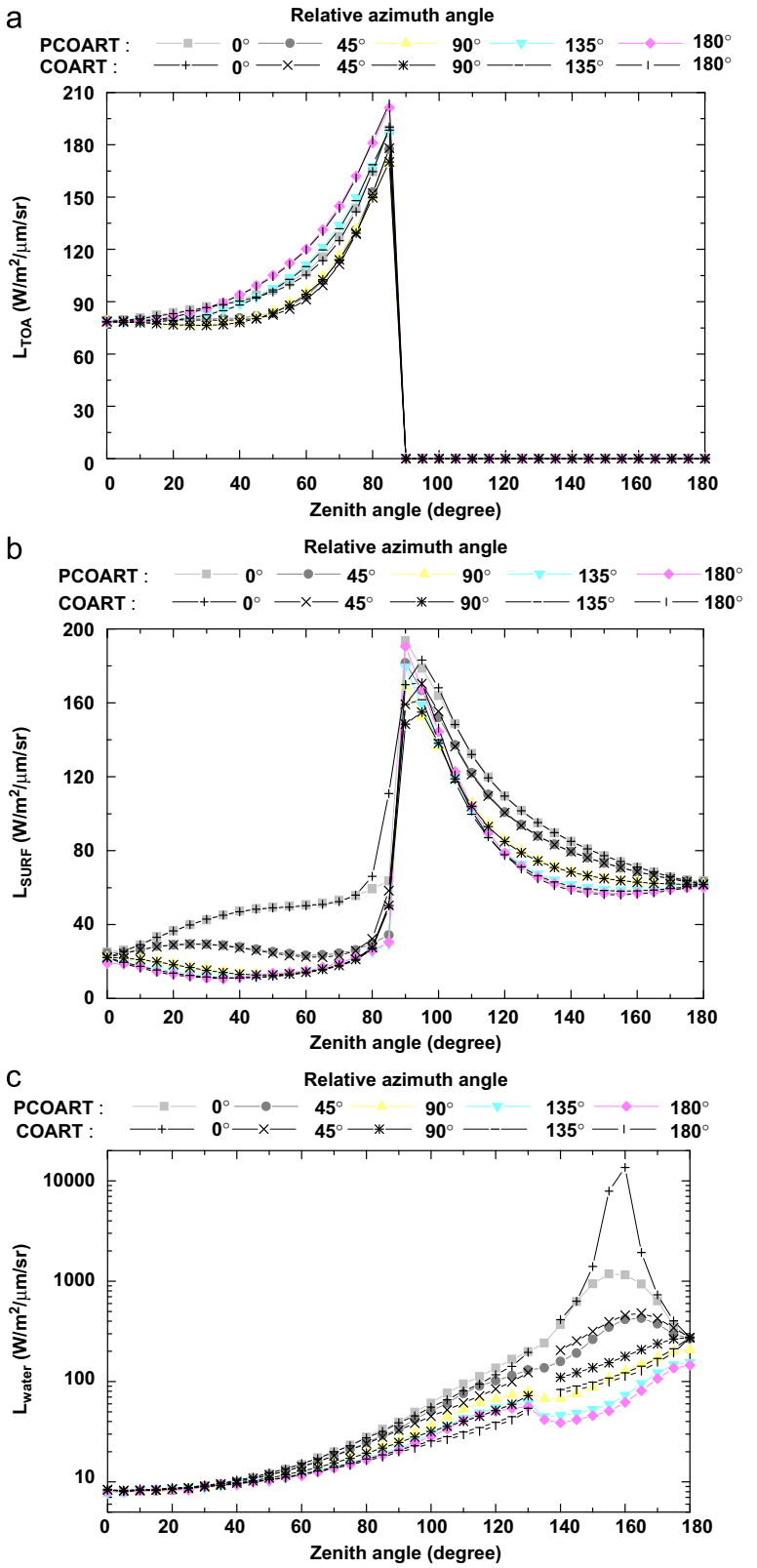

Fig. 11. Comparison of the 412 nm radiance fields at top-of-atmosphere, just above sea surface and 5 m depth underwater between PCOART and COART with the horizontal wind speeds at a height of 10 m above the sea surface of 15 m/s. (a) Top-of-atmosphere, (b) just above sea surface, (c) 5 m depth underwater.

Gaussian-quadrature point. For any case, the upward radiance at 5 m depth underwater is in good agreement between PCOART and COART, which is more important for the application of ocean color remote sensing. The results are the same for the horizontal wind speeds at a height of 10 m above the sea surface of 15 m/s, as shown in Fig. 11.

3.4. Validation by the polarizing remote sensing data of POLDER

We use the polarizing remote sensing data of POLDER onboard the ADEOS-II satellite to validate the capacity of the POCART to simulate the linear polarizing radiance at the top-of-atmosphere. To compare the linear polarization radiance between the PCOART prediction and POLDER measurements, the input parameters of the PCOART should mostly be similar to the reality of the atmosphere and ocean optical properties when POLDER is measured. However, it is difficult to determine the optical properties of aerosol exactly because of its large spatio-temporal variation. Therefore, the lesser the aerosol impact, the more reliable the comparison result. Generally, the blue band has a larger Rayleigh scattering and a relatively smaller contribution of the aerosol scattering than that at a longer wavelength. Therefore, to avoid the effect of the aerosol scattering contribution furthest, the shortest wavelength band, 443 nm band of POLDER, is selected in the simulation. In the simulation, the atmosphere–ocean system is discretized into three homogeneous layers with the atmosphere molecular layer (or Rayleigh scattering layer) in the top layer, and aerosol in the middle layer, and ocean in the lower layer. Here we only consider the linear polarizing radiance at the top-of-atmosphere. Because the water-leaving radiance is almost unpolarized, we assume the ocean is total absorption. Thirty Gaussian-quadrature points in atmosphere are used in the simulation by PCOART. The Rayleigh optical thickness is 0.2326 for the 443 nm band of POLDER, and the aerosol optical thickness is inversed by the 865 nm band of POLDER using the single scattering approximate method as [23]

$$\tau_a = \frac{4\pi L_a \cos\theta_S}{\omega_a F_0[P_a(\vartheta_-)+(\rho(\theta_0)+\rho(\theta_S))P_a(\vartheta_+)]} \tag{78}$$

where θ_S is the sensor observation zenith angle; θ_0 is the solar zenith angle; F_0 is solar irradiance; L_a is the aerosol scattering radiance; ω_a is the aerosol single scattering albedo; P_a is the aerosol scattering phase function; ρ is the reflection coefficient of the flat sea surface, which can be calculated by Eq. (58), and ϑ is the scattering angle, which can be calculated from solar geometry (θ_0,φ_0) and sensor observation geometry (θ_v,φ_v) as

$$\cos\vartheta_\pm = \pm\cos\theta_0\cos\theta_v - \sin\theta_0\sin\theta_v\cos(\varphi_v-\varphi_0) \tag{79}$$

ω_a and P_a are determined by the aerosol model, and here we use the M80 aerosol model (Marine aerosol with a relative humidity of 80%). Because the water-leaving radiance at 865 nm wavelength can be neglected, the L_a is approximated by L_a=L_t−L_r, where L_t is the total radiance received by POLDER, and L_r is the Rayleigh scattering radiance.

Fig. 12 shows the comparison of the linear polarization reflectance (*LPR*) at 443 nm between the PCOART predictions and the POLDER measurements on 10 July 2003. The LPR is defined as

$$LPR = \frac{\pi\sqrt{Q^2+U^2}}{F_0\cos\theta_0} \tag{80}$$

where Q and U are the linear polarization radiances at the top-of-atmosphere. It can be seen that PCOART reproduced the linear polarization reflectance measured by POLDER perfectly. Fig. 13(a) shows the scattering plot comparison of 443 nm *LPR* between POLDER measurements and PCOART predictions on 10 July 2003 with the aerosol optical thickness less than 0.2 and the sensor observation zenith angle less than 30°. We can see the good agreement between POLDER measurements and PCOART predictions with the correlation coefficient of 0.9968 and the standard deviation of 0.0026, and the averaged relative error of 4.96% ($LPR > 0.01$). For the other wavelengths corresponding to the bands of POLDER/ADEOS-II, although the aerosol impact is larger than 443 nm, there is also good agreement between POLDER measurements and PCOART predictions (Fig. 13b), but it results in much more scatter than the result at 443 nm because of the greater influence of the aerosol variation. The above results could benefit other polarizing satellite remote sensors, such as the Aerosol Polarimetry Sensor, which is scheduled to be part of the NASA Glory Mission [50]. It is worthy to note that the present model of PCOART is a one-dimensional layered model, which neglects the horizontal inhomogeneous properties of the real nature. Although the present model of PCOART can perfectly reproduce the linear polarization reflectance measured by POLDER as a whole, the simulation errors of the pixels near clouds may be large, and for these pixels the simulation should consider the three-dimensional effect.

4. Conclusion

We have developed a vector radiative transfer model termed PCOART for the coupled ocean–atmosphere system with rough sea-surface. The model solves the vector radiative transfer equation using the matrix-operator (or adding-doubling) method. In order to couple the radiative transfer in the atmosphere and ocean, the infinite thin ocean–atmosphere interface layer is added to deal with the reflection and transmission through the sea surface. Both the flat and wind induced rough sea surface cases are implemented in the PCOART.

Several radiative transfer problems in the atmosphere and ocean are used to validate the model, including the radiative transfer problem of Rayleigh atmosphere, the standard radiative transfer problems in ocean, the coupled ocean–atmospheric

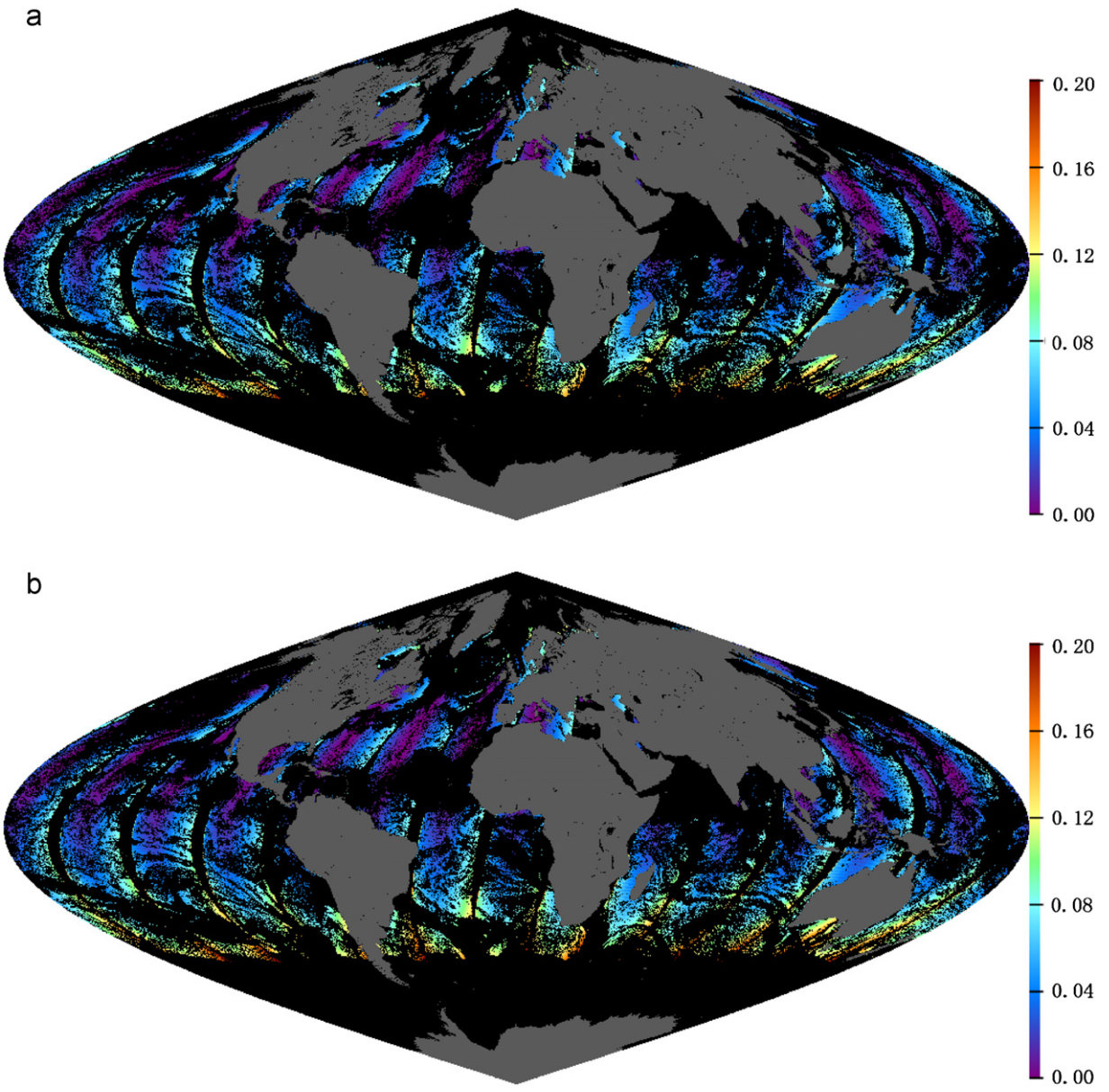

Fig. 12. Comparison of the 443 nm linear polarization reflectance between POLDER measurements and PCOART predictions on 10 July 2003. (a) POLDER measurements, (b) PCOART predictions.

radiative transfer problem, and the simulation of the linear polarizing radiance measured by POLDER. Validation results of the radiative transfer problem of Rayleigh atmosphere show that the Stokes vector calculated by PCOART for the rough sea-surface is exact, where the relative errors of the first component of Stokes vector calculated by PCOART are all less than 0.5% for the different observation zenith angles and relative azimuth angles, and the components *Q*, *U*, and *V* of the Stokes vector calculated by PCOART are consistent well with the results of the exact Rayleigh scattering look-up tables of MODIS.

In order to assess the performance of PCOART in applying to the underwater radiative transfer problems, a model intercomparison was performed for five well-defined standard problems covering specific aspects of the radiative transfer in the ocean for both the flat and rough sea surface. The results show that there were good agreements between the PCOART predictions and the standard values for both the highly scattering and absorbing cases, which present that PCOART can exactly predict the underwater radiance fields for the sharp forward scattering, stratified, finite depth and rough sea surface cases. Meanwhile, a model intercomparison was performed to assess the performance of PCOART when applied to the radiative transfer problem of the coupled ocean–atmosphere system. The scalar radiative transfer code named COART was used to validate the numerical accuracy of the radiance fields in the atmosphere and ocean calculation by PCOART for

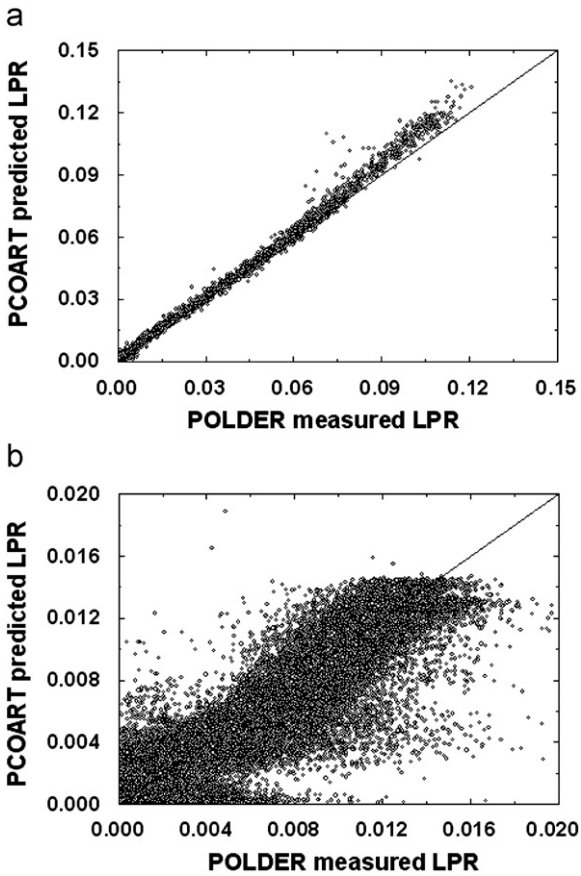

Fig. 13. Scatter plot comparisons of the linear polarization reflectance between POLDER measurements and PCOART predictions on 10 July 2003. (a) 443 nm, (b) 865 nm.

rough sea-surface. The same radiative transfer problem of coupled ocean–atmosphere system for rough sea-surface was calculated both by PCOART and by COART. The results show that there are good agreements between PCOART and COART results for the radiance fields at the top-of-atmosphere and just above the sea surface. For the radiance field at 5 m depth underwater, there is a large difference of the downward radiance around the solar refraction direction where PCOART results are much smaller than COART, which is caused by the forward scattering radiance reduction effect of the Delta-M processing in PCOART. However, there is good agreement between PCOART and COART for the upward radiance at 5 m depth underwater, which is more important for the application of ocean color remote sensing. Finally, the satellite remote sensing data of the linear polarization radiance measured by POLDER is used to test the capacity of PCOART to simulate the polarization radiance at top-of-atmosphere for satellite remote sensing application. The results show that PCOART can reproduce the linear polarization reflectance measured by POLDER perfectly, and there is good agreement between POLDER measurements and PCOART predictions with the correlation coefficient of 0.9968 and the standard deviation of 0.0026, and the averaged relative error of 4.96% ($LPR > 0.01$) for the 443 nm band of POLDER.

To the best of the authors' knowledge, there are few codes dealing with the vector radiative transfer in the coupled ocean–atmosphere system for rough sea surface. PCOART can not only simulate the total radiance field in the coupled ocean–atmosphere system with wind induced rough sea surface exactly but also predict the polarization radiance field both in the atmosphere and in the ocean correctly, which can serve as a useful tool for the ocean optics and ocean color remote sensing communities.

Acknowledgements

The POLDER datasets were obtained from the French Space Agency. This work was supported by the National Basic Research Program of China (973 Program, Grant no. 2009CB421202), the National Natural Science Foundation of China (Grant nos. 40976110 and 40706061) and the National High Technology Research and Development Program of China

(863 Program, Grant nos. 2007AA12Z137 and 2008AA09Z104). The authors thank the reviewers for their valuable suggestions.

References

[1] Gordon HR, Wang V. Retrieval of water-leaving radiance and aerosol optical thickness over the oceans with SeaWiFS: a preliminary algorithm. Appl Opt 1994;33:443–52.
[2] Jin Z, Charlock TP, Rutledge K. Analysis of broadband solar radiation and albedo over the ocean surface at COVE. J Ocean Atmos Tech 2002;19: 1585–601.
[3] Plass GN, Kattawar GW, Catchings FE. Matrix operator theory of radiative transfer. I: Rayleigh scattering. Appl Opt 1973;12:314–29.
[4] Stamnes K, Conklin P. A new multi-layere discrete ordinate approach to radiative transfer calculations in anisotropically scattering atmospheres. J Quant Spect Rad Trans 1984;31:273–82.
[5] Karp AH, Greenstadt JJ, Filmore AJ. Radiative transfer through an arbitrary thick scattering atmosphere. J Quant Spect Rad Trans 1980;24:391–406.
[6] Collins DG, Blattner WG, Wells MB, Horak HG. Backward Monte-Carlo calculations of polarization characteristics of the radiation emerging from a spherical shell atmosphere. Appl Opt 1972;11:2684–705.
[7] Mishchenko MI, Travis LD. Satellite retrieval of aerosol properties over the ocean using polarizations as well as intensity of reflected sunlight. J Geophys Res 1997;102:16989–7013.
[8] Chandrasekhar S. Radiative transfer. Clarendon Press Oxford; 1950.
[9] Irvine WM. Multiple scattering in planetary atmospheres. Icarus 1975;25:175–204.
[10] Garcia RDM, Siewert CE. The FN method for radiative transfer models that include polarization effects. J Quant Spect Rad Trans 1989;41:117–45.
[11] Kisselev VB, Roberti L, Perona G. Finite-element algorithm for radiative transfer in vertically inhomogeneous media: numerical scheme and applications. Appl Opt 1995;34:8460–71.
[12] Stamnes K, Tsay SC, Wiscombe W, Jayaweera K. Numerically stable algorithm for discrete-ordinate-method radiative transfer in multiple scattering and emitting layered media. Appl Opt 1988;27:2502–9.
[13] Mobley V. Light and water: radiative transfer in natural water. San Diego: Academic Press; 1994.
[14] Plass GN, Humphreys TJ, Kattawar GW. Ocean–atmosphere interface: its influence on radiation. Appl Opt 1981;20:917–30.
[15] Kattawar GW, Adams CN. Stokes vector calculations of the submarine light field in an atmosphere–ocean with scattering according to a Rayleigh phase matrix: effect of interface refractive index on radiance and polarization. Limnol Oceanogr 1989;34:1453–72.
[16] Adams CN, Kattawar GW. Effect of volume-scattering function on the errors induced when polarization is neglected in radiance calculations in an atmosphere–ocean system. Appl Opt 1993;32:4610–7.
[17] Mishchenko MI, Lacis AA, Travis LD. Errors induced by the neglect of polarization in radiance calculations for Rayleigh-scattering atmospheres. J Quant Spect Rad Trans 1994;51:491–510.
[18] Lacis A, Chowdhary J, Mishenko MI, Cairns B. Modeling errors in diffuse-sky radiation: vector vs scalar treatment. Geophys Res Lett 1998;25:135–8.
[19] Chami M, Defoin-Platel M. Sensitivity of the retrieval of the inherent optical properties of marine particles in coastal waters to the directional variations and the polarization of the reflectance. J Geophys Res 2007;112:C05037, doi:10.1029/2006JC003758.
[20] Chami M. Importance of the polarization in the retrieval of oceanic constituents from the remote sensing reflectance. J Geophys Res 2007;112:C05026, doi:10.1029/2006JC003843.
[21] Cariou J, Le Jeune B, Lotrian J, Guern Y. Polarization effects of seawater and underwater targets. Appl Opt 1990;29:1689–95.
[22] Waterman TH. Polarization patterns in submarine illumination. Science 1954;120:927–32.
[23] Gordon HR, Brown JW, Evans RH. Exact Rayleigh scattering calculations for use with the Nimbus-7 coastal zone color scanner. Appl Opt 1988;27:862–71.
[24] Gordon HR, Du T, Zhang T. Atmospheric correction of ocean color sensors: analysis of the effects of residual instrument polarization sensitivity. Appl Opt 1997;36:6938–48.
[25] Meister G, Kwiatkowska EJ, Franz BA, Patt FS, Feldman GC, McClain CR. Moderater-resolution imaging spectroradiometer ocean color polarization correction. Appl Opt 2005;44:5524–35.
[26] Nakajima T, Tanaka M. Effect of wind-generated waves on the transfer of solar radiation in the atmosphere–ocean system. J Quant Spect Rad Trans 1983;29:521–37.
[27] Fischer J, Grassl H. Radiative transfer in an atmosphere–ocean system: an azimuthally dependent matrix operator approach. Appl Opt 1984;23:1032–9.
[28] Fell F, Fischer J. Numerical simulation of the light field in the atmosphere–ocean system using the matrix-operator method. J Quant Spect Rad Trans 2001;69:351–88.
[29] Jin Z, Charlock TP, Rutledge K, Stamnes K, Wang Y. Analytical solution of radiative transfer in the coupled atmosphere–ocean system with a rough surface. Appl Opt 2006;45:7443–55.
[30] Bulgarelli B, Kisselev VB, Roberti L. Radiative transfer in the atmosphere–ocean system: the finite-element method. Appl Opt 1999;38:1530–42.
[31] Chami M, Santer R, Dilligeard E. Radiative transfer model for the computation of radiance and polarization in an ocean–atmosphere system: polarization properties of suspended matter for remote sensing. Appl Opt 2001;40:2398–416.
[32] Zhai P, Hu Y, Trepte RC, Lucker PL. A vector radiative transfer model for coupled atmosphere and ocean systems based on successive order of scattering method. Opt Express 2009;17:2057–79.
[33] Zhai P, Hu Y, Chowdhary J, Trepte CR, Lucker PL, Josset DB. A vector radiative transfer model for coupled atmosphere and ocean systems with a rough interface. J Quant Spect Rad Trans, doi:10.1016/j.jqsrt.2009.12.005, 2010.
[34] You Y, Zhai P, Kattawar GW, Yang P. Polarized radiance fields under a dynamic ocean surface: a three-dimensional radiative transfer solution. Appl Opt 2009;48:3019–29.
[35] Sommersten ER, Lotsberg JK, Stamnes K, Stamnes JJ. Discrete ordinate and Monte Carlo simulations for polarized radiative transfer in a coupled system consisting of two media with different refractive indices. J Quant Spect Rad Trans 2010;111:616–33.
[36] Ota Y, Higurashi A, Nakajima T, Yokota T. Matrix formulations of radiative transfer including the polarization effect in a coupled atmosphere–ocean system. J Quant Spect Rad Trans 2010;111:878–94.
[37] Chowdhary J, Cairns B, Travis LD. Contribution of water-leaving radiances to multiangle, multispectral polarimetric observations over the open ocean: bio-optical model results for case 1 waters. Appl Opt 2006;45:5542–67.
[38] He X, Pan D, Bai Y, Zhu Q, Gong F. Vector radiative transfer numerical model of coupled ocean–atmosphere system using matrix-operator method. Sci China SerD 2007;50(3):442–52.
[39] Evans KF, Stephens L. A new polarized atmospheric radiative transfer model. J Quant Spect Rad Trans 1991;46:413–23.
[40] Mishchenko MI, Travis LD, Lacis AA. Multiple scattering of light by particles. New York: Cambridge University Press; 2006.
[41] Hovenier JW, Van der Mee C, Domke H. Transfer of polarized light in planetary atmospheres: basic concepts and practical methods. Dordrecht, The Netherlands: Kluwer; 2004.
[42] Cox C, Munk W. Measurements of the roughness of the sea surface from photographs of the sun's glitter. J Opt Soc Am 1954;44:838–50.
[43] Gordon HR, Wang M. Surface-roughness considerations for atmospheric correction of ocean color sensors. I: the Rayleigh-sacttering component. Appl Opt 1992;31:4247–60.
[44] Young AT. Revised depolarization corrections for atmospheric extinction. Appl Opt 1980;19:1333.

[45] Mobley CD, Bernard G, Gordon HR, Jin Z, Kattawar GW, Morel A, et al. Comparison of numerical models for computing underwater light fields. Appl Opt 1993;32:7484–503.
[46] Petzold TJ. Volume scattering functions for selected ocean waters. SIO Ref. 72–78 (Scripps Institution of Oceanography, La Jolla, CA, 1972).
[47] Wiscombe WJ. The Delta-M method: rapid yet accurate radiative flux calculations for strongly asymmetric phase functions. J Atmos Sci 1977;34:1408–22.
[48] Stamnes K, Tsay SC, Laszlo I. DISORT, a general-purpose Fortran program for Discrete-Ordinate-Method radiative transfer in scattering and emitting layered media: Documentation of Methodology version 1.1, March 2000, available as "DISORTReport1.1.pdf" at 〈ftp://climate1.gsfc.nasa.gov/wiscombe/Multiple_Scatt/〉.
[49] Nakajima T, Tanaka M. Algorithms for radiative intensity calculations in moderately thick atmosphere using a truncation approximation. J Quant Spect Rad Trans 1988;40:51–69.
[50] Mishchenko MI, Cairns B, Kopp G, Schueler CF, Fafaul BA, Hansen JE, et al. Accurate monitoring of terrestrial aerosols and total solar irradiance introducing the glory mission. Bull Am Meteorol Soc 2007;88:677–91.